

# Long Term Simulations Of Astrophysical Jets; Energy Structure and Quasi-Periodic Ejection

Ahmed IBRAHIM

*Kwasan Observatory, Kyoto University, Yamashina-ku, Kyoto 607-8471*

*aaeakf1@kwasan.kyoto-u.ac.jp*

and

Kazunari SHIBATA

*Kwasan Observatory, Kyoto University, Yamashina-ku, Kyoto 607-8471*

*shibata@kwasan.kyoto-u.ac.jp*

(Received 2006 December 31; accepted 2007 February 10)

## Abstract

We have performed self-consistent 2.5-dimensional nonsteady MHD numerical simulations of jet formation as long as possible, including the dynamics of accretion disks. Although the previous nonsteady MHD simulations for astrophysical jets revealed that the characteristics of nonsteady jets are similar to those of steady jets, the calculation time of these simulations is very short compared with the time scale of observed jets. Thus we have investigated long term evolutions of mass accretion rate, mass outflow rate, jet velocity, and various energy flux. We found that the ejection of jet is quasi-periodic. The period of the ejection is related to the time needed for the initial magnetic field to be twisted to generate toroidal field

$$T_{ejection} \propto \frac{1}{V_A} \propto \frac{1}{B} \propto E_{mg}^{-\frac{1}{2}}.$$

We compare our results with both the steady state theory and previous 2.5-dimensional nonsteady MHD simulations. Then it is found that time averaged velocity of jets ( $V_{jet\ ave}$ ) are  $\sim 0.1V_K$  and  $\sim 0.1V_{jet\ max}$ , where  $V_K$  is the Keplerian velocity at  $(r, z) = (1, 0)$  and  $V_{jet\ max}$  is the maximum velocity of jet. Nevertheless, the characteristics of our simulations are consistent with those of steady solution and previous short term simulations in that the dependences of the time averaged velocity  $V_{z\ ave}$  and mass outflow rate  $\dot{M}_{w\ ave}$  on the initial magnetic field strength are approximately

$$\dot{M}_{w\ ave} \propto B^{0.32} \quad \text{and} \quad V_{jet\ ave} \propto B_0^{0.3}.$$

**Key words:** MHD Numerical simulation, astrophysical jet

## 1. Introduction

Astrophysical jets have been observed in young stellar objects (YSOs) (e.g., Fukui et al. 1993; Ogura 1995; Burrows 1996; Bachiller 1996; Reipurth et al. 2002; Curiel et al. 2006), active galactic nuclei (AGNs) (e.g., Bridle & Perley 1984; Biretta et al. 1995; Junor et al. 1999; Jiang & Hong 2003; Matthew 2005), and some X-ray binaries (XRBs) (e.g., Margon 1984; Mirabel et al. 1994; Tingay et al. 1995; Kotani et al. 1996; Migliari et al. 2006). Although the acceleration and collimation mechanisms of these jets are still not well understood, these objects are believed to have accretion disks in their central regions.

The standard model of a jet-disk system has been an original idea of Blandford & Payne (1982). Energy and angular momentum are removed magnetically from the accretion disk by field lines anchored to the disk surface and extending to large distances. Blandford & Payne (1982) showed that a centrifugally driven outflow of matter from the disk is possible, if the angle between field line and disk is less than  $60^\circ$ . They discussed self-similar solutions of the steady and axisymmetric MHD equations and the possibility of such acceleration and collimation of the flow from a cold Keplerian disk. After their work, many authors studied MHD models of jet formation from accretion disks (e.g., Pudritz & Norman 1986; Sakurai 1987; Lovelace et al. 1991; Contopoulos & Lovelace 1994; Najita & Shu 1994; Fendt & Camenzind 1996) based on the theory of steady and axisymmetric MHD winds, which was first developed by Weber & Davis (1967) for the solar wind. Cao & Spruit (1994) examined the mass outflow rate of magnetically driven jets by studying the solution that passes through the slow magnetosonic point (see also Li 1995). They confirmed that the inclination angle of the field line is very important for achieving a high mass outflow rate.

Kudoh & Shibata (1995, 1997a) studied one-dimensional steady magnetically driven jets along a fixed poloidal field line for a wide range of parameters, assuming the shape of that field line. They found that the steady solutions generally can be classified into two branches: (1) magneto-centrifugally driven jets, when the magnetic field is strong, in that case they found that the jet velocity ( $V_{jet}$ ) and mass outflow rate ( $\dot{M}_w = \frac{dM_w}{dt}$ ) depend on the magnetic energy ( $E_{mg}$ ) as  $V_{jet} \propto B_0^{1/3}$ ,  $\dot{M}_w \sim \text{constant}$  and (2) magnetic pressure-driven, when the magnetic field is weak, in that case  $V_{jet} \propto B_0^{1/6}$ ,  $\dot{M}_w \propto B_0^{0.5}$ . In the centrifugal case, the main acceleration occurs before the flow speed exceeds the Alfvén speed, while in the latter case most of the acceleration occurs after the flow speed becomes greater than the Alfvén speed. This mass flux scaling law was confirmed by Ustyugova et al. (1999).

In most theoretical models of jets from accretion disks, however, accretion disks are treated as boundary conditions. Accretion disks only play a role of supplying energy and mass to the jets, and neither accretion flow nor internal structure of disks are considered in these models. Since the disk itself is not treated, such simulations may last over hundreds of Keplerian periods. This idea was first applied by Ustyugova et al. (1995). Extending this work,

Romanova et al. (1997) found a stationary final state of a slowly collimating disk wind in the case of a spilt-monopole initial field structure after 100 Keplerian periods. Ouyed & Pudritz (1997a, 1997b) presented time-dependent simulations of the jet formation from a Keplerian disk. For a certain (already collimating) initial magnetic field distribution, a stationary state of the jet flow was obtained after about 400 Keplerian periods of the inner disk with an increased degree of collimation. Ouyed et al. (2003) investigate the problem of jet stability and magnetic collimation extending the axisymmetric simulations to 3D.

On the other hand, Uchida & Shibata (1985) and Shibata & Uchida (1987, 1989, 1990) performed time-dependent, two-dimensional axisymmetric (2.5-dimensional) MHD numerical simulations of magnetically driven jets from accretion disks. They solved the interaction between a geometrically thin rotating disk, including the dynamics of the disk, and a large-scale magnetic field that was initially uniform and vertical. Shibata & Uchida (1986) investigated the detailed properties of these jets. They found that (1) the velocity of the jet was typically of order of the disk's Keplerian velocity and (2) it increased with increasing magnetic field strength in a manner similar to the scaling law of Michel's (1969) solution. Matsumoto et al. (1996) carried out 2D MHD simulations of a torus threaded by poloidal magnetic fields and found that (1) the jet velocities were again comparable to the Keplerian velocity and (2) the mass outflow rate of the jet increased with the strength of the initial magnetic field. Kudoh et al (1998) studied the formation mechanism of jets from geometrically thick disks and the dependence of the initial magnetic field strength ( $B_0$ ) in detail by performing self-consistent 2.5-dimensional, nonsteady, ideal MHD simulations including the dynamics of the disk. They found that the ejection point is determined by the effective potential resulting from the gravitational and centrifugal forces along the field lines (Blandford & Payne 1982) and also that the velocity and mass outflow rate are consistent with those predicted by the steady theory (Kudoh & Shibata 1995 and Kudoh & Shibata 1997a). Kato et al (2002) performed 2.5-dimensional, axisymmetric, ideal MHD simulations of jets from geometrically thin disks for Keplerian and sub-Keplerian cases over a wide range of initial magnetic field strengths. Kigure & Shibata (2005) investigate the problem of jet formation and stability by using 3-dimensional MHD simulations. To investigate the stability of the MHD jet, they introduce a perturbation to the accretion disk with a nonaxisymmetric sinusoidal or random fluctuation of rotational velocity. In both perturbation cases, a nonaxisymmetric structure with  $m = 2$  appears in the jet, where  $m$  is the azimuthal wavenumber. They conclude that this structure seems to originate in the accretion disk.

On the other hand, the acceleration and collimation of the jet have been studied in the steady (e.g. Sauty et al. 2004; Bogovalov & Tsinganos 2005). In recent years, many simulations taking other physical processes into consideration, e.g. the magnetic diffusion (Kuwabara et al. 2000, Kuwabara et al. 2005; Fendt & Čemeljić 2002; Casse & Keppens 2002, Casse & Keppens 2004), the dynamo process in the accretion disk (von Rekowski et al.

2003), and the radiation force ( Proga 2003), have been performed. Koide et al. (1999) showed that a magnetically driven jet in the general relativistic MHD simulation has characteristics similar to those of the nonrelativistic MHD jet (Shibata & Uchida 1986). In addition to these studies which consider the initial magnetic field as large scale, several papers were considering the evolution of a stellar magnetic dipole in interaction with a diffusive accretion disk. Hayashi et al. (1996) observed magnetic reconnection and evolution of X-ray flares during the first rotational periods in their numerical simulations.

We note that all calculations including the treatment of the disk structure and the ideal MHD, (e.g. Shibata & Uchida 1986, Shibata & Uchida 1987, Shibata et al. 1989, Shibata & Uchida 1990; Matsumoto et al. 1996; Kudoh et al. 1998; Kato et al. 2002; Kudoh et al. 2002 and Kigure & Shibata 2005), could be performed only for 1 – 2 Keplerian periods of inner disk. At this point, we emphasize that the observed kinematic time scale of protostellar jets can be as large as  $10^3$  –  $10^4$  yrs, corresponding to  $5 \times 10^4$  –  $5 \times 10^5$  stellar rotational periods (and inner disk rotations)! For example, proper motion measurements for HH30 jet (Burrows 1996) give a knot velocity of about  $100$  –  $300 \text{ km s}^{-1}$  and a knot production rate of about 0.4 knot per year. Assuming a similar jet velocity along the whole jet extending a long 0.25 pc (López et al. 1995), the kinematic age is about 1000 yrs

In order to have access to the observed time scale of jets and to know whether the jet formation becomes quasi-steady state, we performed long term 2.5-dimensional MHD simulations of jets.

We solve the dynamics of the disk as in Shibata & Uchida (1986), Kudoh et al. (1998) and their following studies. We also want to know whether the time averaged physical quantities have the same characteristics as those in the steady model and previous simulations (Kudoh et al. 1998) and (Kato et al. 2002). Our calculation time is about 20 times longer than those of previous simulations. Also, the simulation box is large enough to minimize the effect of top and side boundary conditions

## 2. Numerical Method

### 2.1. Assumptions

Our simulations make the following assumptions: (1) axial symmetry around the rotational axis ( $\partial/\partial\varphi = 0$ ), including the azimuthal components of a velocity ( $v_\varphi$ ) and a magnetic field ( $B_\varphi$ ) (i.e., 2.5-dimensional approximation); (2) ideal MHD (i.e., Ohmic diffusivity and/or ambipolar diffusion are assumed to be negligible); (3) an inviscid perfect gas with a specific heat ratio of  $\gamma = 5/3$ ; (4) a point-mass gravitational potential only, with disk self-gravity neglected.

### 2.2. Basic Equations

The basic equations we use are the 2.5-dimensional ideal MHD equations in cylindrical coordinates  $(r, \varphi, z)$  :

$$\frac{\partial \rho}{\partial t} + v_r \frac{\partial \rho}{\partial r} + v_z \frac{\partial \rho}{\partial z} = -\rho \left( \frac{1}{r} \frac{\partial}{\partial r} (r v_r) + \frac{\partial v_z}{\partial z} \right), \quad (1)$$

$$\begin{aligned} \frac{\partial v_r}{\partial t} + v_r \frac{\partial v_r}{\partial r} + v_z \frac{\partial v_r}{\partial z} &= -\frac{1}{\rho} \frac{\partial p}{\partial r} + \frac{v_\varphi^2}{r} - \frac{\partial \Psi}{\partial r} - \frac{1}{4\pi\rho} \\ &\quad \times \left[ B_z \frac{\partial B_z}{\partial r} + \frac{B_\varphi}{r} \frac{\partial}{\partial r} (r B_\varphi) \right] + \frac{B_z}{4\pi\rho} \frac{\partial B_r}{\partial z}, \end{aligned} \quad (2)$$

$$\frac{\partial (r v_\varphi)}{\partial t} + v_r \frac{\partial (r v_\varphi)}{\partial r} + v_z \frac{\partial (r v_\varphi)}{\partial z} = \frac{1}{4\pi\rho} \left[ B_r \frac{\partial}{\partial r} (r B_\varphi) + B_z \frac{\partial}{\partial z} (r B_\varphi) \right], \quad (3)$$

$$\begin{aligned} \frac{\partial v_z}{\partial t} + v_r \frac{\partial v_z}{\partial r} + v_z \frac{\partial v_z}{\partial z} &= -\frac{1}{\rho} \frac{\partial p}{\partial r} + \frac{\partial \Psi}{\partial r} - \frac{1}{4\pi\rho} \\ &\quad \times \left( B_r \frac{\partial B_r}{\partial z} + B_\varphi \frac{\partial B_\varphi}{\partial z} \right) + \frac{B_r}{4\pi\rho} \frac{\partial B_z}{\partial r}, \end{aligned} \quad (4)$$

$$\frac{\partial e}{\partial t} + v_r \frac{\partial e}{\partial r} + v_z \frac{\partial e}{\partial z} = -\frac{p}{\rho} \left[ \frac{1}{r} \frac{\partial}{\partial r} (r v_r) + \frac{\partial v_z}{\partial z} \right], \quad (5)$$

$$e = \frac{p}{(\gamma - 1)\rho}, \quad (6)$$

$$\frac{\partial B_r}{\partial t} = -\frac{\partial}{\partial z} (v_z B_r - v_r B_z), \quad (7)$$

$$\frac{\partial B_\varphi}{\partial t} = \frac{\partial}{\partial z} (v_\varphi B_z - v_z B_\varphi) - \frac{\partial}{\partial r} (v_r B_\varphi - v_\varphi B_r), \quad (8)$$

$$\frac{\partial B_z}{\partial t} = \frac{1}{r} \frac{\partial}{\partial r} \left[ r (v_z B_r - v_r B_z) \right], \quad (9)$$

where  $\Psi = -GM/(r^2 + z^2)^{1/2}$  is the gravitational potential,  $G$  is the gravitational constant, and  $M$  is the mass of a central object. Other variables are summarized in Table 1.

### 2.3. Initial Conditions

As an initial condition, we assume an equilibrium disk rotating in a central point-mass gravitational potential (Matsumoto et al. 1996). Exact solutions for these conditions can be obtained under the simplifying assumptions for the distribution of angular momentum and pressure (e.g., Abramowicz et al. 1978):

$$L = L_0 r^a, \quad (10)$$

$$p = K \rho^{1+1/n}. \quad (11)$$

Then the distribution of material in the disk is given by

$$\Psi = -\frac{GM}{(r^2 + z^2)^{1/2}} + \frac{1}{2(1-a)} L_0^2 r^{2a-2} + (n+1) \frac{p}{\rho} = \text{constant}. \quad (12)$$

We use  $a = 0.45$  and  $n = 3$  throughout this paper. These are the different parameters from the previous similar simulations (e.g., Kudoh et al. 1998, Kato et al. 2002). Our parameters make the disk thicker and wider than that of Kato et al. (2002), mainly for both numerical

convenience and long term simulation. The mass distribution outside the disk is assumed to be that of a uniformly high temperature corona in hydrostatic equilibrium without rotation. The density distribution in hydrostatic equilibrium is

$$\rho = \rho_c \exp \left\{ \alpha \left[ \frac{r_0}{(r^2 + z^2)^{1/2}} - 1 \right] \right\}. \quad (13)$$

where  $r_0$  is a radius defined later (see Table 1),  $\alpha = (\gamma V_{k0}^2 / V_{sc}^2)$ ,  $V_{sc}$  is the sound velocity in the corona,  $V_{k0} = (GM/r_0)^{1/2}$  is the Keplerian velocity at radius  $r_0$ . We use  $\alpha = 1$  and  $\rho_c/\rho_0 = 10^{-3}$  throughout this paper, where  $\rho_0$  is a density defined later (see Table 1).

For simplicity, the initial magnetic field is assumed to be uniform and parallel to the axis of rotation

$$B_z = B_0 = \text{constant}, \quad B_r = B_\varphi = 0. \quad (14)$$

Indeed, the presence of a large-scale magnetic field in accretion-disk-jet systems is observed in AGN jets and protostellar jets (Ray et al. 1997; Pushkarev et al. 2005; Gabuzda et al. 2004; Wouter et al. 2006) and is assumed theoretically in jet launching models (e.g. Casse & Keppens 2004, and references therein)

#### 2.4. Boundary Conditions

On the axis ( $r = 0$ ) we assume a boundary condition that is symmetric for  $\rho, p, v_z$ , and  $B_z$  while  $v_r, v_\varphi, B_r$ , and  $B_\varphi$  are antisymmetric.

The side, top and bottom surfaces are free boundaries. In order to avoid a singularity at the origin, the region around  $r = z = 0$  is treated by softening the gravitational potential as

$$\Psi = \begin{cases} -GM/(r^2 + z^2)^{1/2} & \text{for } \epsilon < (r^2 + z^2)^{1/2}, \\ -GM1/\epsilon - [(r^2 + z^2)^{1/2} - \epsilon]/\epsilon^2 & \text{for } 0.5\epsilon < (r^2 + z^2)^{1/2} \leq \epsilon, \\ -1.5GM/\epsilon & \text{for } (r^2 + z^2)^2 \leq 0.5\epsilon. \end{cases} \quad (15)$$

We use  $\epsilon = 0.2r_0$  throughout this paper.

These boundary conditions are different from those MHD simulations of jets from accretion disks performed by Ouyed et al (1997a), Romanove et al. (1997), Meier et al. (1997), Ustyugova et al. (1999), and Pudritz et al. (2006). The main difference is the condition on the equatorial plane. They assumed an inflowing fixed boundary condition (i.e., the angular momentum is continually injected from the boundary). Therefore, their numerical simulations did not allow disk accretion due to magnetic braking nor growth of magneto-rotational instability.

#### 2.5. Numerical Schemes

The numerical schemes we use are the cubic-interpolated pseudo-particle (CIP) method (Yabe & Aoki 1991; Yabe et al. 1991) and the method of characteristics-constrained transport (MOCCT) (Evans & Hawley 1988; Stone & Norman 1992). The magnetic induction equation is solved using MOCCT and the others using CIP. This is the two-dimensional version of the scheme used by Kudoh & Shibata (1997b), and Koide et al. (1999)

## 2.6. Parameter

We normalize the physical quantities with their initial value at  $(r, z) = (r_0, 0)$  taking  $r_0 = (L_0^2/GM)^{1/(1-2\alpha)}$  so that the initial density of the disk has maximum value of  $\rho_0$  at  $(r, z) = (r_0, 0)$ . The normalized unit for each variable is summarized in Table 1. There are two nondimensional parameters:

$$E_{\text{th}} = \frac{V_{s0}^2}{\gamma V_{K0}^2}, \quad (16)$$

$$E_{\text{mg}} = \frac{V_{A0}^2}{V_{K0}^2}, \quad (17)$$

where  $V_{s0} = (\gamma p_0/\rho_0)^{1/2}$ ,  $V_{A0} = B_0/(4\pi\rho_0)^{1/2}$ , and  $p_0$  is the initial pressure at  $(r, z) = (r_0, 0)$ . The initial parameters we use in this paper are summarized in Table 2. We use  $E_{\text{th}} = 0.018$  throughout this paper. When  $E_{\text{th}} = 0.018$  and  $\alpha = 1$ , the temperature of corona is about  $10^2$  times greater than that of the disk at  $(r, z) = (r_0, 0)$ . In this paper, we adopt  $L = L_0 r^{0.45}$  ( $L_0 = 1.00$ ) that makes the disk thicker and wider than that of Kato et al. (2002), mainly for both numerical convenience and long term simulation: the internal structure of a thick disk is better resolved than that of a thin disk, and much matter in the disk can make the time of simulations longer than that of Kudoh et al. (1998). Of course, many accretion disks in YSOs, AGNs, and XRBs are expected to be geometrically thin and nearly Keplerian. Kato et al. (2002) also performed simulations for geometrically thin disk case. However they calculated only one or two orbits just the same as Kudoh et al. (1998). The minimum grid size is  $0.05r_0$  in  $r$ -direction and  $0.01r_0$  in  $z$ -direction. The maximum grid size in  $r$ -direction is  $0.1r_0$  and  $0.4r_0$  in  $z$ -direction, and the number of grid points used in this paper is  $269 \times 639$ . The grid spacing is uniform for  $r/r_0 < 1$  and  $z/r_0 < 1$  and stretched in  $r$  and  $z$  for  $r/r_0 > 1$  or  $z/z_0 > 1$ . The size of the computational domain is  $(R_{\text{min}}/r_0 \sim R_{\text{max}}/r_0, Z_{\text{min}}/r_0 \sim Z_{\text{max}}/r_0) = (0.0 \sim 24.8, -65.75 \sim 65.75)$ .

## 3. Numerical Results

### 3.1. Typical Case

Figures 1, 2 and 3 shows the time evolution of the density distribution (color scales, top panels), temperature distribution (color scales, bottom panels) ( $T \equiv \gamma p/\rho$ ), poloidal magnetic field lines, and poloidal velocity (hereafter, the variables are expressed in nondimensional form) for model 1,4 and 6 respectively. Time  $t = 2\pi \simeq 6.28$  corresponds to one Keplerian orbit at  $(r, z) = (1, 0)$ . Evolutions for all models look like similar each other.

Now we show the case of model 4 (see Figure 2). In the early stage of evolution, a torsional Alfvén wave is generated at the disk surface and propagates up into the corona ( $t = 13$ ). Since this wave extracts angular momentum, the rotating disk begins to fall into the central region. The surface layer of the disk falls faster than the equatorial part. This is the avalanche-like accretion that was studied by Matsumoto et al. (1996). Because only a small fraction of the

accreted matter is ejected into the bipolar direction due to Lorentz force in the relaxing twist, both density and pressure of the inner region increase. Within this region, angular momentum is transferred from the high to the low-density parts. The cold material on the disk surface is ejected as a jet ( $t = 35$ ). At  $t = 82$  due to the magnetorotational instability the channel flow becomes clear. Initially both gas pressure and magneto-centrifugal force drives and accelerates the outflow (below the Alfvén surface). After that, when the toroidal field generated as a result of the differential rotation of the accretion disk is accumulated, the acceleration is due to the magnetic pressure gradient,  $\partial(B_\varphi^2/8\pi)/\partial z$ . To illustrate the twist level of the magnetic field lines, we show in figure 4 the time variation of the ratio of the toroidal magnetic field,  $B_\varphi$ , to the poloidal magnetic field,  $B_p$ , along  $r = 0.225$ . Figure 4 illustrates that in case of initial weak magnetic field the twisting field  $B_\varphi$  become more dominant and both of the Alfvén point and the slow point become near to the accretion disk (Pelletier & Pudritz 1992 and Kudoh & Shibata 1997a). In both the weak and strong initial magnetic field a strong twist appears at  $t=15$  and propagates outward when the jet is ejected.

The outflow consists of both the material that is initially in the corona and the material from the disk. Channel flow continues to grow in the disk and jets are ejected continuously and intermittently ( $t = 82$ ). Jet ejection and accretion still continue at the last stage of evolution in our simulations ( $t = 115$ ). We can also see that magnetic field lines entwine each other and that the magnetic turbulent flow develops. We can see that the magnetic islands are created by magnetic reconnections in the disk. Since we assumed ideal MHD, the magnetic reconnection is caused by numerical diffusion. Numerical diffusion is inevitable for finite difference numerical schemes, even though we do not include the magnetic diffusivity explicitly. The time evolution is similar to that in Matsumoto et al. (1996) and Kudoh et al. (1998).

The avalanche-like flow is caused by a physical mechanism similar to that of the magnetorotational instability (Balbus & Hawley 1991; Hawley & Balbus 1991). Note that although the disk is initially rotating in our model, the corona is not. The discontinuity of azimuthal velocity at the interface between them generates torsional Alfvén waves propagating into both the corona and the disk. Since the Alfvén wave behaves like a large amplitude perturbation, it triggers the magnetorotational instability in the disk. The wavelength of this instability is determined by the most unstable wavelength ( $\lambda$ ) for the magnetorotational instability,  $\lambda \sim 2\pi V_A/\Omega$ , so the base height of the avalanche depends on the initial magnetic field strength.

#### 4. Time Evolutions of Some Physical Quantities of Jets

One of the most important purpose of this study is to clarify whether the jet ejection becomes steady state. In figures 5,6 and 9 we show the time evolutions of the mass outflow rate ( $\dot{M}_w$ ), the mass accretion rate ( $\dot{M}_a$ ), and the toroidal magnetic field energy ( $E_{mgt}$ ) for model 1 ( $E_{mg} = 2 \times 10^{-4}$ ), model 4 ( $E_{mg} = 2 \times 10^{-5}$ ) and model 6 ( $E_{mg} = 2 \times 10^{-6}$ ).  $\dot{M}_w$  is defined by

$$\dot{M}_w = \pi \left( \int_0^1 \rho v_z(r, z=z_p) r dr - \int_0^1 \rho v_z(r, z=-z_p) r dr \right). \quad \text{at } z = 4. \quad (18)$$

where  $z_p$  is z-coordinates for jets to pass through. The mass accretion rate for various models.  $\dot{M}_a$  is defined by

$$\dot{M}_a = -\pi \int_{-1}^1 \rho v_r(r=1.0, z) r dz. \quad (19)$$

It is not easy to define  $(\dot{M}_w)$  and  $(\dot{M}_a)$ , because of following reasons: (1) ejection and accretion are very nonsteady, and sometimes the ejected matter falls back onto the disk, (2) when initial magnetic field is weak, the jet ejection point goes away from the equatorial plane after long time simulation. Kudoh et al. (2002) and Kuwabara et al. (2000) found that mass accretion and mass ejection take place intermittently in the case without perturbation in the disk. The simulation time of both of them ranged from one orbit in case of Kuwabara et al. (2000) and three orbits in case of Kudoh et al. (2002). Our simulations in this paper more than 20 orbits for different models. From Figure 5, it is clear that the mass ejection flux is still intermittent until the last stage of evolution. The intermittent ejection is clear in all models in the figure 5 but there are some differences between them. The first one, in case of strong magnetic field the intermittency is almost similar at the beginning of the simulation to that at the end of simulation. But in case of weak field, as the simulation goes on, the ejection mass flux becomes very nonsteady. Not only the intermittency increases in case of weak magnetic field but also the absolute amount of mass flux increases. But in case of strong magnetic field we notice the opposite. Figure 6 shows the mass accretion rate for models 1, 4 and 6. The mass accretion, like mass ejection, is intermittent until the last stage of our simulations. In both weak and strong initial magnetic field the mass accretion is intermittent. The general trend of intermittency of the mass accretion is similar to the intermittency of mass ejection. That similarity is more clearer for example in model 4 than other models. In model 4 the absolute value of mass accretion at the beginning of simulation is smaller than that at the end. We notice the trend in the mass ejection, also the same trend happen in the other models.

Because of the mass accretion rate is highly variable, plotting it at one radius in time shows very little of the overall characters of the accretion. We therefore show values that are averaged over space or time, in order to obtain a better understanding of the overall accretion within the disk.

Figure 7 shows the accretion rate against time, averaged between  $r = 0.52$  and  $r = 10$ . This region is chosen since the accretion has little value at larger radii. This shows that even though the accretion rate is highly intermittent, it is predominantly positive. The behavior of the accretion is more complex in case of weak initial magnetic field after 10 orbits, because the evolution of the disk take a long time until it becomes more turbulent. The accretion, in case of strong initial magnetic field, is positive during the first 5 orbits. During that time, part of the subtracted angular momentum is ejected as a jet. The other part is transported at large

distances by the magnetic stresses. This is exactly what we see in Figure 8, which shows the accretion rate as a relation of radius of the disk, averaged over the first 10 orbits. Accordingly, we see that the accretion is positive in the inner part of the disk and the accretion is negative beyond the radius 2-4. The negative accretion continue about 5 orbits. The accretion becomes positive again because the continuous ejection of the jet which means continuous subtraction of the angular momentum.

Figure 9 shows the toroidal magnetic energy for model 1, 4 and 6. The toroidal magnetic field energy  $E_{mgt}$  for various models is defined by

$$E_{mgt} = \pi \left( \int_0^1 \frac{B_{\varphi(r,z=z_p)}^2}{8\pi} r dr + \int_0^1 \frac{B_{\varphi(r,z=-z_p)}^2}{8\pi} r dr \right) / \pi \int_0^1 2r dr. \quad (20)$$

The intermittency is clear and the trend is also similar to mass ejection. Hence we try to find the relation between mass accretion, ejection and magnetic field. The ejections are intermittent and seem to have periods for all models, and the periodicity seems different in the models with different initial magnetic field. Next we check the times of ejection peaks for different models and study the relation between that peak times with the time needed for the toroidal field to be accumulated after that untwisted in vertical direction carrying the mass flux. From the initial conditions equation 14,  $B_z = B_0 = \text{constant}$ ,  $B_r = B_{\varphi} = 0$ . With the rotation of the disk by angular velocity  $\Omega$ , the toroidal field  $B_{\varphi}$  is generated from  $B_z$ .

$$\frac{\partial B_{\varphi}}{\partial T} \approx \Omega B_z. \quad (21)$$

By integration w.r.t. time  $T$  then

$$B_{\varphi} \approx \Omega B_z T. \quad (22)$$

The ejection occurs when the magnetic energy equals the rotational energy, then

$$\frac{B_{\varphi}^2}{8\pi} \approx \frac{1}{2} \rho V_{\varphi}^2 \approx \frac{1}{2} \rho V_k^2. \quad (23)$$

Combining Eqs. 22 and 23, yields

$$\frac{\Omega^2 B_z^2 T^2}{8\pi} \approx \frac{1}{2} \rho V_{\varphi}^2 \approx \frac{1}{2} \rho V_k^2, \quad (24)$$

$$T_{ejection} \approx \frac{\sqrt{4\pi\rho}}{B_z} \frac{V_k}{\Omega} \approx \frac{1}{V_A} \frac{V_k}{\Omega}, \quad (25)$$

$$T_{ejection} \propto \frac{1}{V_A} \propto \frac{1}{B} \propto E_{mg}^{-\frac{1}{2}}, \quad (26)$$

where  $V_A$  is the Alfvén speed,  $B$  is the initial magnetic field strength and  $T_{ejection}$  is the time corresponding to the peak mass ejection rate as shown in Figure 10. Figure 11 shows the relation between the initial magnetic field strength and the average time interval between the peaks of the mass ejection rate of models 1, 3, 4 and 6. Here the squares correspond to our numerical values and the solid line is the best fit to them with the following dependence

$$T_{average,eje} \propto E_{mg}^{-0.3}.$$

The dotted line corresponds to the analytical relation equation 26. We notice that the dependence of the ejection time on the initial magnetic field ( $E_{mg}$ ) is in a good agreement with our analytical expectation equation 26. The small deviation from the analytical relation comes from our assumption that both the magnetic field and density will remain constant during the simulation. But the real situation is that both the density and magnetic field increase with time during the simulation. By taking the time evolution of both density and magnetic into account (inside the disk), the equation 25 becomes

$$T_{ejection} \propto \frac{\sqrt{\rho}}{B_z} \propto \frac{1}{V_A}. \quad (27)$$

Both the density and  $B_z$  component of the magnetic field increase steeply in case of strong initial magnetic field. On the other hand, the density almost remains constant in case of initial weak magnetic field while  $B_z$  increases. Then as  $B_z$  increases with time the ejection time becomes shorter than if we consider constant initial magnetic field. But the time evolution of the density will make an opposite effect in that case of strong initial magnetic field i. e. the effect of the increase of  $B_z$  will be weakened by the effect of the increase in  $\rho$ . On the other hand, in the case of initial weak magnetic field, the effect of the increase of the density is too small to weaken the effect of the increase of magnetic field. Hence the evolution effect of  $B_z$  is more prominent in case of weak initial magnetic field. So we think that the evolution of both density and magnetic field  $B_z$  may explain the discrepancy between the analytical dependence of the ejection time and the initial magnetic field. Consequently, when we consider the average magnetic field instead of the initial magnetic field in Figure 11a, the agreement is more better as we can see from Figure 11b. In that case the best fit is

$$T_{average,eje} \propto E_{mg}^{-0.36}.$$

## 5. Time averaged Velocities and Mass Outflow Rates of Jets As a Function of Magnetic Energy

There is also an interesting question regarding magnetically driven jets: how the velocities and mass outflow rates depend on the strength of the magnetic field. Figure 12a shows the time averaged jet velocities ( $V_{jet\ ave}$ ) as a function of the initial magnetic field  $E_{mg}$ .  $V_{jet\ ave}$  is defined by

$$V_{jet\ ave} = \int_0^{T_e} \int_0^4 v_z(r, z=z_p) dr dt / 10T_{orbit}, \quad . \quad (28)$$

where  $T_e$  is the end of the simulation time,  $T_{orbit}$  is the time of one disk rotation and  $10T_{orbit}$  is the sum of the time over which the speed of the jet is averaged. The figure shows that *the jet velocity is  $10^{-1}$  smaller than that of order the Keplerian speed* for a wide range of  $E_{mg}$  in the disk and that its dependence on  $E_{mg}$  as shown in Figure 12a is approximately.

$$V_{jet\ ave} \propto E_{mg}^{0.15}.$$

Figure 12b shows the maximum jet velocities ( $V_{jet \ max}$ ) as a function of the initial magnetic field  $E_{mg}$ . The solid line shows

$$V_{jet \ max} \propto E_{mg}^{0.17}.$$

Figure 12c and 12d show the time averaged jet velocities ( $V_{jet \ ave}$ ) and maximum jet velocities respectively as a function of  $E_{mg}/\dot{M}_w$ . The solid line shows

$$V_{jet \ ave} \propto (E_{mg}/\dot{M}_w)^{0.16}.$$

$$V_{jet \ max} \propto (E_{mg}/\dot{M}_w)^{0.17}.$$

It is interesting that (in case of weak magnetic field) this relation shows an approximate agreement with the scaling law of the Michel's solution (Michel 1969; Belcher & MacGregor 1976); i.e.,  $v_\infty = (\Phi^2 \Omega_F^2 / \dot{M}_w)^{1/3}$ ,

where  $v_\infty$  is the poloidal velocity at infinity and  $\Phi = r_0^2 B_0$  and  $\Omega_F$  is proportional to the Keplerian angular velocity of the disk.

Figure 13a shows the time averaged mass accretion rates of the disk as a function of the initial  $E_{mg}$ . The figure shows that its dependence on  $E_{mg}$  is about

$$\dot{M}_a \propto E_{mg}^{0.6}.$$

Figure 13b shows the time averaged mass ejection rates of our jets as a function of the initial  $E_{mg}$ . Its dependence on  $E_{mg}$  is approximately

$$\dot{M}_w \propto E_{mg}^{0.16}.$$

Figure 13c shows the time averaged toroidal magnetic energy as a function of the initial  $E_{mg}$ . Its dependence on  $E_{mg}$  is approximately

$$E_{mgt} \propto E_{mg}^{0.5}.$$

Figure 13d shows the ratio of the time averaged mass outflow rate of the jet to the time averaged mass accretion rate of the disk as a function of the initial  $E_{mg}$ .  $\dot{M}_w/\dot{M}_a$  is of order of 0.1 or less

$$\dot{M}_w/\dot{M}_a \propto E_{mg}^{-0.4}.$$

### 5.1. Long time evolution of jet velocity

Figure 14 shows the long time evolution of jet velocity which is calculated through the jet region  $r = 0 - 1$ . Figure 14(a) shows the averaged jet velocity and Figure 14(b) shows the maximum jet velocity. Both the averaged jet velocity and maximum jet velocity never reach steady state and both of them have the same character of the variation. In case of strong initial magnetic field the jet velocity has the maximum value earlier than the weak initial magnetic field case, but after the first 5 orbits the jet velocity becomes similar for all initial magnetic field. After the first 10 orbits the jet velocity for the initial weak magnetic field becomes higher than that in case of strong initial magnetic field case.

We notice that in all models the jet velocity decreases severely after the first three orbits. We think that the high velocity of the jet in the first stage of evolution is result from both the effect of initial and boundary condition. Also, at the first stage of the simulation the position of the ejection point of the jet is near the gravitational center. With the simulation going on the density and pressure of the central region of disk increases which leads to the decrease or stopping the accretion within that region. As a result for that the position of the ejection point of the jet becomes far from the gravitational center so that the jet velocity decreases. Also, The effect of softening gravitational potential near the gravitational center leads to the decrease of the jet velocity. While the simulation goings on, the magnetic field lines are trapped inside the softening gravitational potential. Consequently, they lose their angular momentum and their rotational velocities become very small which leads to the decrease of the jet velocity.

### 5.2. Jet driving forces

Fig. 15 shows the time evolution of powers of the jet i.e. Poynting flux  $F_{p,j}$ , kinetic flux  $F_{k,j}$  and enthalpy flux  $F_{en,j}$  which are described as:

$$F_{p,j} = - \int_0^1 2\pi r \frac{c}{4\pi} (E \times B)_z dr \quad \text{at } z = 4, \quad (29)$$

$$F_{k,j} = \int_0^1 2\pi r \rho v^2 v_z dr \quad \text{at } z = 4, \quad (30)$$

$$F_{en,j} = \int_0^1 2\pi r \rho v_z \left( \frac{\gamma}{\gamma-1} \frac{p}{\rho} \right) dr \quad \text{at } z = 4, \quad (31)$$

where  $z$  is z-coordinates for jets to pass through.

The Poynting flux  $F_{p,j}$  plays the dominant effect in driving and accelerating the jet at the initial evolution of our simulation of a strong magnetic field case, (model 1)  $E_{mg} = 2 \times 10^{-4}$  unit  $t = 50$ , after that it is suddenly becoming very weak.

In case of initial weak magnetic field, model 5,  $E_{mg} = 5 \times 10^{-6}$ , during the initial stage of the evolution, the enthalpy flux is the dominant one until  $t \sim 50$ , and both kinetic flux and Poynting flux have nearly the same value. After  $t \sim 50$ , the dominant energy flux is the Poynting flux and the other two fluxes have nearly the same value. At the last stage of the evolution the Poynting flux decreases again and the enthalpy flux becomes the dominant one. In case of very weak initial magnetic field , model 9,  $E_{mg} = 2 \times 10^{-7}$ , the enthalpy flux is the dominant one until the last stage of the simulation except after  $t \sim 225$  it decreases sharply.

Figure 16 shows the relation between the average enthalpy flux  $F_{en,j \text{ ave}}$ , kinetic flux  $F_{k,j \text{ ave}}$  and Poynting flux  $F_{p,j \text{ ave}}$  and the initial magnetic field strength. The average is defined as;

$$F_{p,j \text{ ave}} = - \int_0^{T_e} \int_0^1 2\pi r \frac{c}{4\pi} (E \times B)_z dr dt / 10T_{crit} \quad \text{at } z = 4, \quad (32)$$

$$F_{k,j \text{ ave}} = \int_0^{T_e} \int_0^1 2\pi r \rho v^2 v_z dr dt / 10T_{crit} \quad \text{at } z = 4, \quad (33)$$

$$F_{en,j \text{ ave}} = \int_0^{T_e} \int_0^1 2\pi r \rho v_z \left( \frac{\gamma}{\gamma-1} \frac{p}{\rho} \right) dr dt / 10T_{crit} \quad \text{at } z = 4, \quad (34)$$

where  $T_e$  is the end of the simulation time and  $10T_{crit}$  is the sum of the time over which the flux of the jet is averaged. Figure 8 shows that the averaged enthalpy flux have the same value whatever is the initial magnetic field strength, whereas both the averaged kinetic flux and averaged Poynting flux increase with increasing the initial magnetic field.

Kudoh & Shibata (1997a) showed that the dominant energy of a jet depends on the strength of the magnetic field. When the poloidal component of the magnetic field is  $B_p \propto r^{-2}$ , the fast magnetosonic point appears far from the Alfvén point and the dominant energy of the jet is the Poynting flux. In our simulations, the initial magnetic field is uniform. In such models, the fast magnetosonic point locates far from the Alfvén point (Kuwabara et al. 2000).

## 6. Radial jet Structure

Figures 17, 18 and 19 show the radial dependence of mass and energy flux of the jet. The mass flux definition is described by equation 18, the toroidal magnetic energy is described by equation 19 and the Poynting flux, kinetic flux and enthalpy flux are described by equations 32-34 respectively. Figure 17 show the radial profile of the density, poloidal velocity and toroidal field. The radial dependence of density shows that the peak density (which defines the jet) in models 1 and 4 (stronger initial magnetic field cases) is greater than that of model 6 (a weaker initial magnetic field case). The radial dependence of the poloidal velocity shows that the collimated flows show higher velocities closer to the disk axis. The radial dependence of the toroidal magnetic field shows that the maximum value is close to the disk axis as expected for collimated jet. Figure 18 shows the radial profile of the Poynting, enthalpy and kinetic flux. We plot the time averaged flux in annular rings around the symmetry axis (z-axis) to show the radial dependence of these energy flux. We show these radial dependence also by taking different initial magnetic field strength to show its effect. In case of model 4 the collimation of both mass flux and kinetic flux is clear. In figure 18 we calculated the flux at fixed height ( $z=4$ ). Next we will calculate the flux at different heights. At each height we calculate the position of the maximum of each energy flux. Figure 19 shows the r-coordinate versus of z-coordinate of the maximum of mass flux, toroidal energy and kinetic flux for models 1, and 3. This figure shows how the maximum of each flux at different hight progresses in z-direction. From this figure we can notice that the collimation degree is different with the different kind of the flux and the initial magnetic field. In case of strong initial magnetic field the collimation is achieved earlier than weak case. Also the collimation is achieved after some height over the accretion disk.

## 7. Summary and discussion

In this paper we have shown that long term 2.5-dimensional MHD numerical simulation of magnetized accretion flows leads to an intermittent jet like outflow which never reach steady state. Our simulation is an extension of the works of Matusmoto et al. (1996) and Kudoh et al. (1998). Both of them performed time-dependent 2.5-dimensional MHD numerical simulations of jets from accretion disks including the dynamical processes within the disk. They showed that the ejection mechanism of the jets is the same as that in steady theory; i.e. the centrifugal force along the poloidal field line accelerates the jets within an Alfvén radius and, above the Alfvén radius, the jet is accelerated by magnetic pressure. The simulations for both of them last only for one inner disk rotation. What does happen for the characteristics of the jets if the simulations become long?. The answer of this question is given in this paper.

### 7.1. *The Physical Meaning of Time Evolution for $\dot{M}_w$ , $\dot{M}_a$ , and $E_{mgt}$*

Cosmic jets are ubiquitous, being quite often associated with new-born stars, X-ray binaries, active galactic nuclei and gamma-ray bursts. In all such cases , jets and disks seem to be inter-related. Not only jets need disks in order to provide them with the ejected plasma and magnetic fields, but also disks need jets in order that the accreted plasma gets rid of its excess angular momentum to accrete. Observationally, there has already been accumulated enough evidence for such a correlation. For example, in star forming regions an apparent correlation is found between accretion diagnostics and outflow signatures (Hartigan et al. 1995). Hence, our current understanding is that jets are fed by the material of an accretion disk surrounding the central object. The mean controller between the mass accretion rate  $\dot{M}_a$  and the mass ejection rate  $\dot{M}_w$  is the magnetic field strength. Matusmoto et al. (1996) studied the dependence on the initial magnetic field strength. They showed that the ratio of the mass ejected as jet to the total mass of the flux tube was about 10% of the accreting mass. Figure 5 and figure 11 show that time evolution of the mass outflow and toroidal magnetic field outflow is quasi-periodic and the periodicity of the jet can be related to the time needed for the initial magnetic field to be twisted to generate toroidal field. Sato et al. (2003) found that these periodicities are around  $2\pi$ . The toroidal magnetic field energy increases as magnetic field line is twisted and accumulated, because the magnetic field line is dragged with infalling and rotating gases. Then the piled up energy is released by magnetically driven outflow that is triggered by magnetic reconnection so that the mass outflow is intermittent and has some periodicities.

Figure 13d show that the average  $\dot{M}_w$  and  $\dot{M}_a$  (averaged over 10 rotations) is closely related. The magnetic field strength is the controller of the relation between  $\dot{M}_w$  and  $\dot{M}_a$ . When the initial magnetic energy is weak the ratio between  $\dot{M}_w$  and  $\dot{M}_a$  is high. The ratio decreasing with increasing the initial magnetic field. Pelletier & Pudritz (1992) stated that if the disk magnetic field is reduced, there is a very large increase in the mass-loss rate in the wind. The point is that since a slower wind is driven in weaker disk fields, one must provide much

more mass in order to carry off the same amount of disk angular momentum. At strong initial magnetic energy field case the ratio reach a constant value. These dependences are consistent with the results of the steady solution (Kudoh & Shibata 1997a).

### 7.2. The Dependences on the Initial Magnetic Field Strength in the Weak field Case

Kudoh & Shibata (1997a) derived the dependence of the mass outflow rate ( $\dot{M}_w$ ) and mass accretion rate ( $\dot{M}_a$ ) on the initial magnetic field strength using a semi-analytical method,

$$\dot{M}_w \propto E_{\text{mg}}^{1/2}, \quad (35)$$

$$\dot{M}_a \propto E_{\text{mg}}. \quad (36)$$

Furthermore, Michel's scaling law (Michel 1969) is written as

$$V_{\text{jet}} \sim \left( \frac{\Phi^2 \Psi_F^2}{\dot{M}_w} \right)^{1/3} \propto \left( \frac{E_{\text{mg}}}{\dot{M}_w} \right)^{1/3}. \quad (37)$$

On the other hand, we obtain

$$\frac{\dot{M}_{w,\text{ave}}}{\dot{M}_{a,\text{ave}}} \propto E_{\text{mg}}^{-0.4}, \quad (38)$$

$$V_{\text{jet,ave}} \propto E_{\text{mg}}^{0.15}. \quad (39)$$

Our results shown in Figure 12 and Figure 13 are consistent with not only the steady solutions but also the results of both Kudoh et al. (1998), Kato et al. (2002) and Kigure & Shibata (2005). However there is a remarkable difference from the results of Kudoh et al. (1998), Kato et al. (2002) and Kigure & Shibata (2005). They show only maximum values for  $\dot{M}_w$ ,  $\dot{M}_a$  and  $V_z$ , while we examined time-averaged values. We find that  $V_{z \text{ ave}}$  and  $\dot{M}_w$  are 0.1 times smaller than  $V_{z \text{ max}}$  and  $\dot{M}_w \text{ max}$  in the case of Kudoh et al. (1998).

## 8. Conclusions

We have performed time-dependent, 2.5-dimensional, axially symmetric, MHD numerical simulations of jets for many orbital periods. Our simulations solve the dynamical process of the accretion disk for longer time case than that of the previous simulations. Because we wanted to know whether the jet continued to be ejected and become steady (or quasi-steady) state, we investigated time variations of  $\dot{M}_w$ ,  $\dot{M}_a$ , and  $E_{\text{mgt}}$ . We also wanted to know the dependence of  $\dot{M}_{w \text{ ave}}$ ,  $\dot{M}_{a \text{ ave}}$ , and  $V_{z \text{ ave}}$  on the initial magnetic field strength and compared our results with the steady theory and cases of Kudoh et al. (1998) and Kato et al. (2002). We summarize our results as follows:

1. In all models, the ejection of jets is intermittent.
2. The ejection of jets has a period which related to the toroidal field formation.

There are also relationships between  $\dot{M}_w$  and  $\dot{M}_a$ , and between  $\dot{M}_w$  and  $E_{\text{mgt}}$ ; specifically, their time variations are similar.

3. The dependence of  $\dot{M}_w$ ,  $\dot{M}_a$ , and  $E_{mgt}$  on the strength of the initial magnetic field is consistent with those in the steady theory and cases of Kudoh et al. (1998) and Kato et al. (2002). In all cases, however,  $V_{z \text{ ave}}$  and  $\dot{M}_w$  are 0.1 times smaller than  $V_{z \text{ max}}$  and  $\dot{M}_{w \text{ max}}$  in the case of Kudoh et al. (1998) and Kato et al. (2002) and Kigure & Shibata (2005)

#### Acknowledgment

This work is supported by the Grant-in-Aid for the 21st Century COE “Center for Diversity and Universality in Physics” from the Ministry of Education, Culture, Sports, Science and Technology (MEXT) of Japan. Numerical computations were carried out on VPP5000 at the Astronomical Data Analysis Center of the National Astronomical Observatory, Japan (project ID: iaia31c), an inter-university research institute of astronomy operated by the Ministry of Education, Culture, Sports, Science, and Technology.

## References

- Abramowicz, M., Jaroszynski, M., & Sikora, M. 1978, A&A, 63, 221
- Bachiller, R. 1996, ARA&A, 34, 111
- Balbus, S. A., & Hawley, J. F. 1991, ApJ, 376, 214
- Belcher, J. W., & MacGregor, K. B. 1976, ApJ, 210, 498
- Bell, A. R. 1994, Phys. Plasmas, 1, 1643
- Bell, A. R., & Lucek, A. R. 1995, MNRAS, 277, 1327
- Biretta, J. A., Zhou, F., & Owen, F. N. 1995, ApJ, 447, 582
- Bisnovatyi-Kogan, G. S., & Lovelace, R. V. E. 2001, NewA Rev., 45, 663
- Blandford, R. D., & Payne, D. G. 1982, MNRAS, 199, 883
- Bogovalov, S. V., & Tsinganos, K. 2005, MNRAS, 357, 918
- Bridle, A. H., & Perley, R. A. 1984, ARA&A, 22, 319
- Burrows, C. J., et al. 1996, ApJ, 473, 437
- Cao, X., & Spruit, H. C. 1994, A&A, 287, 80
- Casse, F., & Keppens, R. 2002, ApJ, 581, 988
- Casse, F., & Keppens, R. 2004, ApJ, 601, 90
- Contopoulos, J., & Lovelace, R. V. E. 1994, ApJ, 429, 139
- Curiel, S., Ho, P. T. P., Patel, N. A., Torrelles, J. M., Rodriguez, L. F., Trinidad, M. A., Canto, J., Hernandez, L. Gomez, J. F., Garay, G., and Anglada, G. 2006, ApJ, 638, 878
- Evans, C. R., & Hawley, J. F. 1988, ApJ, 332, 659
- Ferrari, A. 1998, ARA&A, 36, 539
- Fendt, C., & Camenzind, M. 1996, A&A, 313, 591
- Fendt, C., & Čemeljić, M. 2002, A&A, 395, 1045
- Frank, A., Lery, T., Gardiner, T. A., Jones, T. W., & Ryu, D. 2000, ApJ, 540, 342
- Fukui, Y., Iwata, T., Mizuno, A., Bally, J., & Lane, A. P. 1993, Protostars and Planets III, ed. E. H. Levy & J. Lunine (Tuscon: Univ. Arizona Press), 603
- Gabuzda, D. C., Murray, E., & Cronin, P. 2004, MNRAS, 351, 89
- Hartigan, P., Edwards, S., Ghandour, L., 1995, ApJ, 452, 736
- Hawley, J. F., & Balbus, S. A. 1991, ApJ, 376, 223
- Hayashi, M. R., Shibata, K., & Matsumoto, R. 1996, ApJ, 468, L37
- Kato, X. S., Kudoh, T., and Shibata, K. 2002, ApJ, 565, 1035
- Jiang, D.R.& Hong, X.Y. 2003, ACTA, 44 Suppl. 282
- Junor W., Biretta J.A., and Livio M. 1999, Nature, 401, 892
- Kigure, H. & Shibata, K. 2005, ApJ, 634, 879
- Koide, S., Shibata, K., & Kudoh, T. 1999, ApJ, 522, 727
- Kotani, T., Kawai, N., Matsuoka, M., & Brinkmann, W. 1996, PASJ, 48, 619
- Krasnopol'sky, R., Li, Z.-Y., & Blandford, R. 1999, ApJ, 526, 631
- Kudoh, T. & Shibata, K. 1995, ApJ, 452, L41
- Kudoh, T. & Shibata, K. 1997a, ApJ, 474, 362
- Kudoh, T. & Shibata, K. 1997b, ApJ, 476, 632
- Kudoh, T., Matsumoto, R. & Shibata, K. 1998, ApJ, 508, 186

- Kudoh, T., Matsumoto, R. & Shibata, K. 2002, PASJ, 54, 121
- Kuwabara, T. Shibata, K., Kudoh, T., & Matsumoto, R. 2000, PASJ, 52, 1109
- Kuwabara, T. Shibata, K., Kudoh, T., & Matsumoto, R. 2005, ApJ, 621, 921
- Li, Z.-Y. 1995, ApJ, 444, 848
- López, J. A., Vázquez, R. & Rodríguez, L. F. 1995, ApJ, 455L..63L
- Lovelace, R. V. E., Berk, H. L., & Contopoulos, J. 1991, ApJ, 379, 696
- Margon, B. 1984, ARA&A, 22, 507
- Matsumoto, R., Uchida, Y., Hirose, S., Shibata, K., Hayashi, M. R., Ferrari, A., Bodo, G., & Norman, C. 1996, ApJ, 461, 115
- Matthew L. Lister, 2005, ASP Conference Series, Vol. 340, 20
- Meier, D. L., Edgington, S., Godon, P., Payne, D. G., & Lind, K. R. 1997, Nature, 388, 350
- Meier, D. L., Koide, S., & Uchida, Y. 2001, Science, 291, 84
- Michel, F. C. 1969, ApJ, 158, 727
- Migliari, S., Tomsick, J. A., Maccarone, T. J., Gallo, E., Fender, R. P., Nelemans, G., and Russell, D. M., 2006, ApJ, 643, L41
- Mirabel, I. F., & Rodriguez, L. F. 1994, Nature, 371, 46
- Najita, J. R., & Shu, F. H. 1994, ApJ, 429, 808
- Ogura, K. 1995, ApJ, 450, L230
- Ouyed, R., & Pudritz, R. E. 1997a, ApJ, 482, 712
- Ouyed, R., & Pudritz, R. E. 1997b, ApJ, 484, 794
- Ouyed, R., & Pudritz, R. E. 1999, MNRAS, 309, 233
- Ouyed, R., Pudritz, R. E., & Stone, J. M. 1997, Nature, 385, 409
- Ouyed, R., Clarke, D., A., & Pudritz, R. E., 2003, ApJ, 582, 292
- Pelletier, G., & Pudritz, R. E. 1992, ApJ, 394, 117
- Proga, D. 2003, ApJ, 585, 406
- Pudritz, R. E., & Norman, C. A. 1986, ApJ, 301, 571
- Pudritz, R. E., Rogers, C. S., and Ouyed, R. 2006, MNRAS, 365, 1131
- Pushkarev, A. B., Gabuzda, D. C., Vetukhnovskaya, Y. N., & Yakimov, V. E. 2005, MNRAS, 356, 859
- Ray, T. P., Musclow, T. W. B., Axon, D. J., et al. 1997, Nature, 385, 415
- Reipurth, B., Heathcote, S., Morse, J., Hartigan, P., & Bally, J. 2002, AJ, 123, 362
- Romanova, M. M., Ustyugova, G. V., Koldoba, A. V., Chechetkin, V. M., & Lovelace, R. V. E. 1997, ApJ, 482, 708
- Sakurai, T. 1987, PASJ, 39, 821
- Sato, K. 2003, Msc. thesis, Kyoto Univ.
- Sauty, C., Trussoni, E., & Tsinganos, K. 2004, A&A, 421, 797
- Shibata, K., & Uchida, Y. 1985, PASJ, 37, 31
- Shibata, K., & Uchida, Y. 1986, PASJ, 38, 631
- Shibata, K., & Uchida, Y. 1987, PASJ, 39, 559
- Shibata, K., & Uchida, Y. 1989, in Theory of Accretion Disks, ed. F. Meyer, W. J. Duschl, J. Frank, & E. Meyer-Hofmeister (Dordrecht: Kluwer), 65

- Shibata, K., & Uchida, Y. 1990, PASJ, 42, 39
- Stone, J. M., & Norman, M. L. 1992, ApJS, 80, 791
- Stone, J. M., & Norman, M. L. 1994, ApJ, 433, 746
- Tingay, S. J., et al. 1995, Nature, 374, 141
- Uchida, Y., & Shibata, K. 1985, PASJ, 37, 515
- Ustyugova, G. V., Koldoba, A. V., Romanova, M. M., Chechetkin, V. M., & Lovelace, R. V. E. 1995, ApJ, 439, L39
- Ustyugova, G. V., Romanova, M. M., Chechetkin, V. M., Lovelace, R. V. E., 1999, ApJ, 516, 221
- von Rekowski, B., Brandenburg, A., Dobler, W., & Shukurov, A. 2003, A&A, 398, 825
- Weber, E. J., & Davis, L., Jr. 1967, ApJ, 148, 217
- Wouter, H. T., Philip, J. D., & Hiroshi, I. 2006, Nature, 440, 58
- Yabe, T., & Aoki, T. 1991, Comp. Phys. Comm., 66, 219
- Yabe, T., Ishikawa, T., Wang, P. Y., Aoki, T., Kadota, Y., & Ikeda, F. 1991, Comp. Phys. Comm., 66, 233

**TABLE 1**  
**UNITS FOR NORMALIZATION**

Normalization	
Physical Quantities	Unit
$t$ (time) .....	$r_0/V_{K0}$
$r, z$ (length) .....	$r_0$
$\rho$ (density) .....	$\rho_0$
$p$ (pressure) .....	$\rho_0 V_{K0}^2$
$v$ (velocity) .....	$V_{K0}$
$B$ (magnetic field) .....	$(\rho_0 V_{K0}^2)^{1/2}$
$e$ (specific internal energy) .....	$V_{K0}^2$

**Table 1.** The unit length  $r_0 = (L_0^2/GM)^{(1/(1-2a))}$  is the radius of the density maximum in the initial disk. The unit velocity  $V_K \equiv (GM/r_0)^{(1/2)}$  is the Keplerian velocity at  $(r, z) = (r_0, 0)$ . The unit density  $\rho_0$  is the initial density at  $(r, z) = (r_0, 0)$ . It is assumed that  $a = 0.45$ , in our study (see eq.12 for the definition of  $a$ )

**TABLE 2**  
**MODEL PARAMETERS**

model	$E_{mg}$	$E_{th}$	time
1	$2 \times 10^{-4}$	0.018	$80.0\pi$
2	$8 \times 10^{-5}$	0.018	$22.1\pi$
3	$5 \times 10^{-5}$	0.018	$31.7\pi$
4	$2 \times 10^{-5}$	0.018	$31.2\pi$
5	$5 \times 10^{-6}$	0.018	$80.0\pi$
6	$2 \times 10^{-6}$	0.018	$37.7\pi$
7	$8 \times 10^{-7}$	0.018	$41.3\pi$
8	$5 \times 10^{-7}$	0.018	$34.8\pi$
9	$2 \times 10^{-7}$	0.018	$80.0\pi$

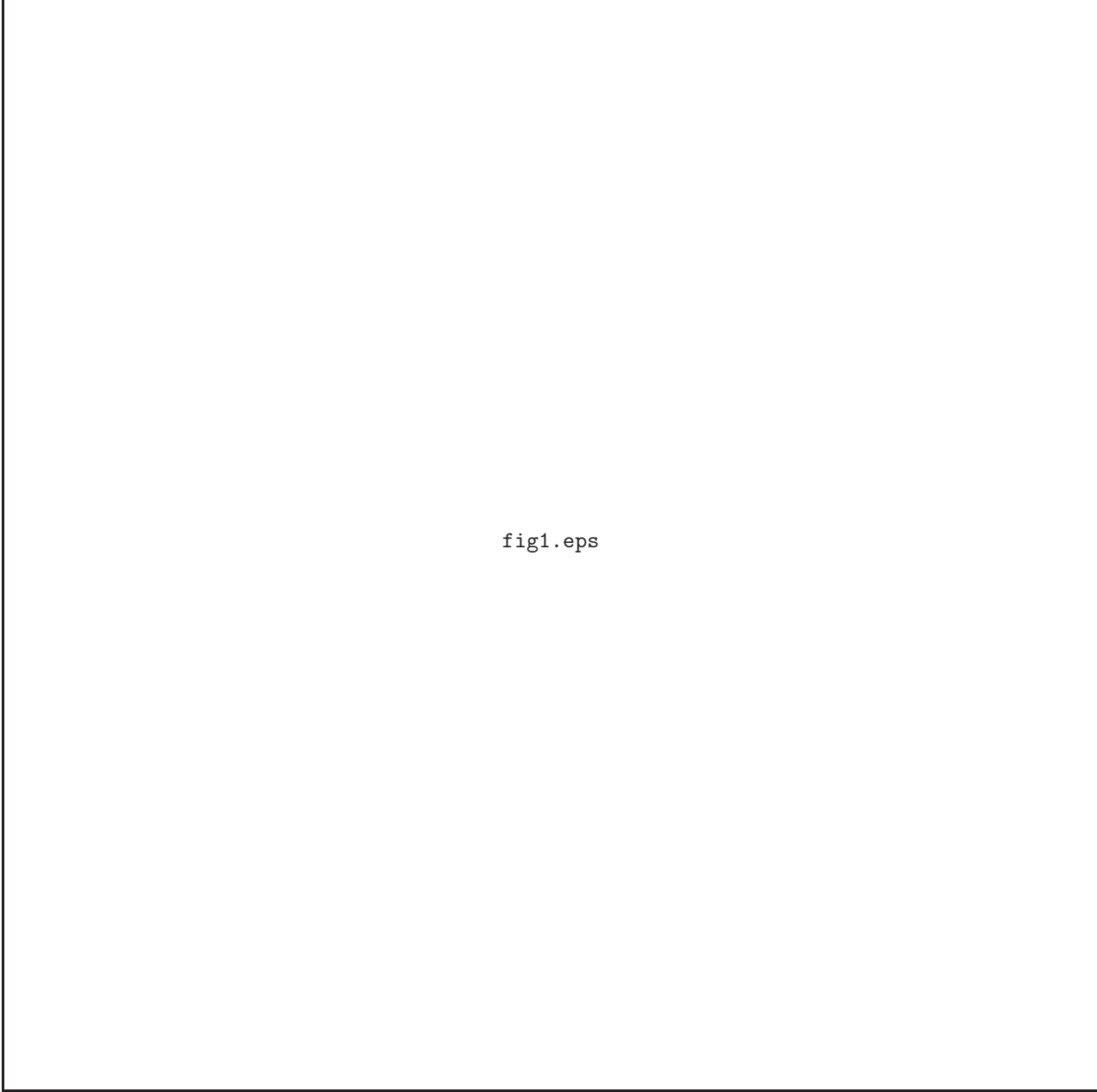


fig1.eps

**Fig. 1.** Temporal evolution of an ideal accretion disk threaded by a poloidal magnetic field. Color levels represent density level (upper panel) and temperature level (bottom panels) while solid lines stand for poloidal magnetic field lines. The time unit labeling each snapshot is for  $t \sim 2\pi \sim 6.28$  corresponds to one Keplerian orbit at  $(r, z) = (1, 0)$ . After a few rotations, outflows are escaping from the disk and the outflow and accretion remain until the last moment of our simulation time. The square refers to the region analyzed by Kudoh et al 1998

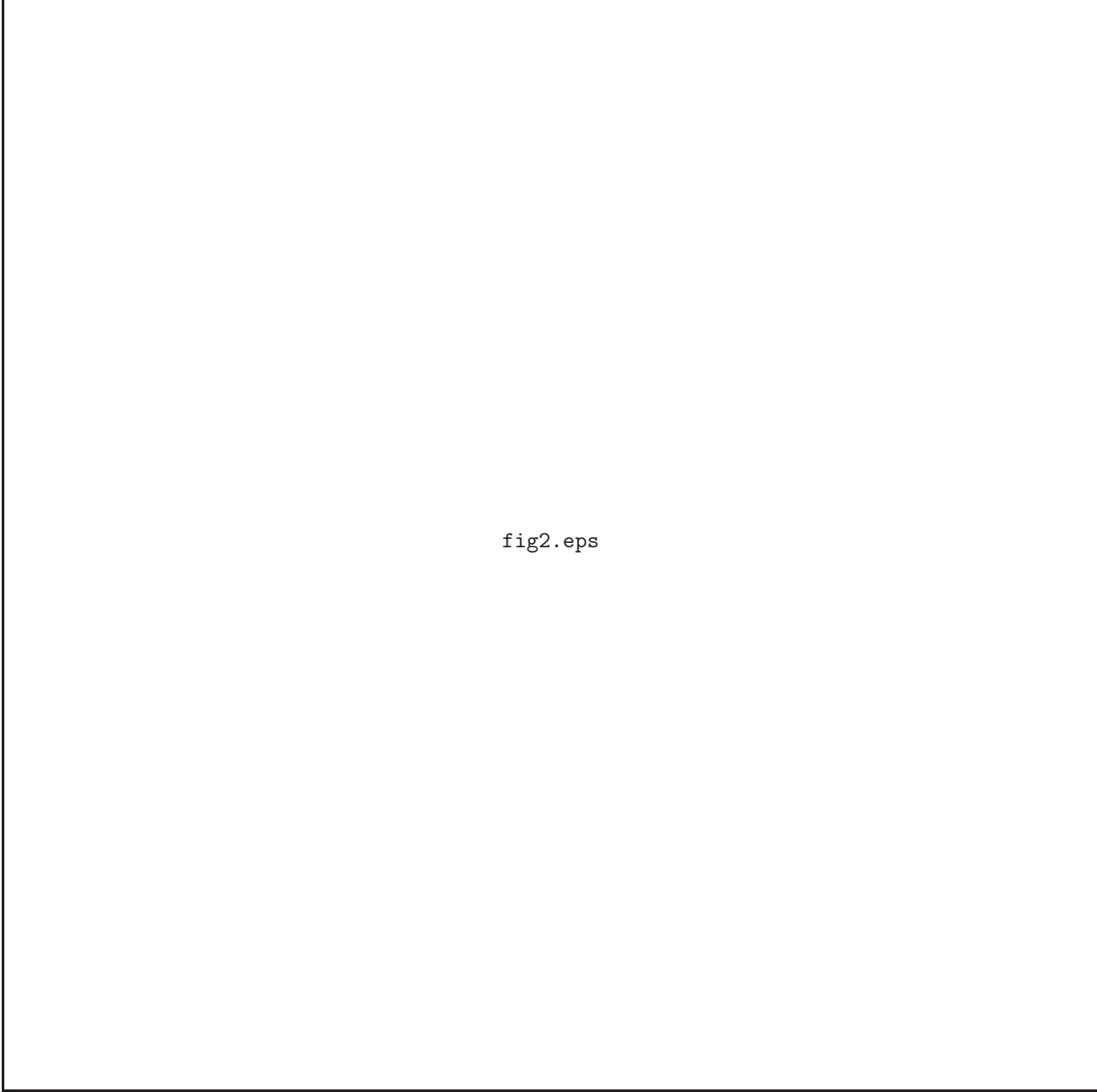


fig2.eps

**Fig. 2.** Temporal evolution of an ideal accretion disk threaded by a poloidal magnetic field. Color levels represent density level (upper panel) and temperature level (lower panel) while solid lines stand for poloidal magnetic field lines. The time unit labeling each snapshot is for  $t \sim 2\pi \sim 6.28$  corresponds to one Keplerian orbit at  $(r, z) = (1, 0)$ . After a few rotations, outflows are escaping from the disk and the outflow and accretion remain until the last moment of our simulation time

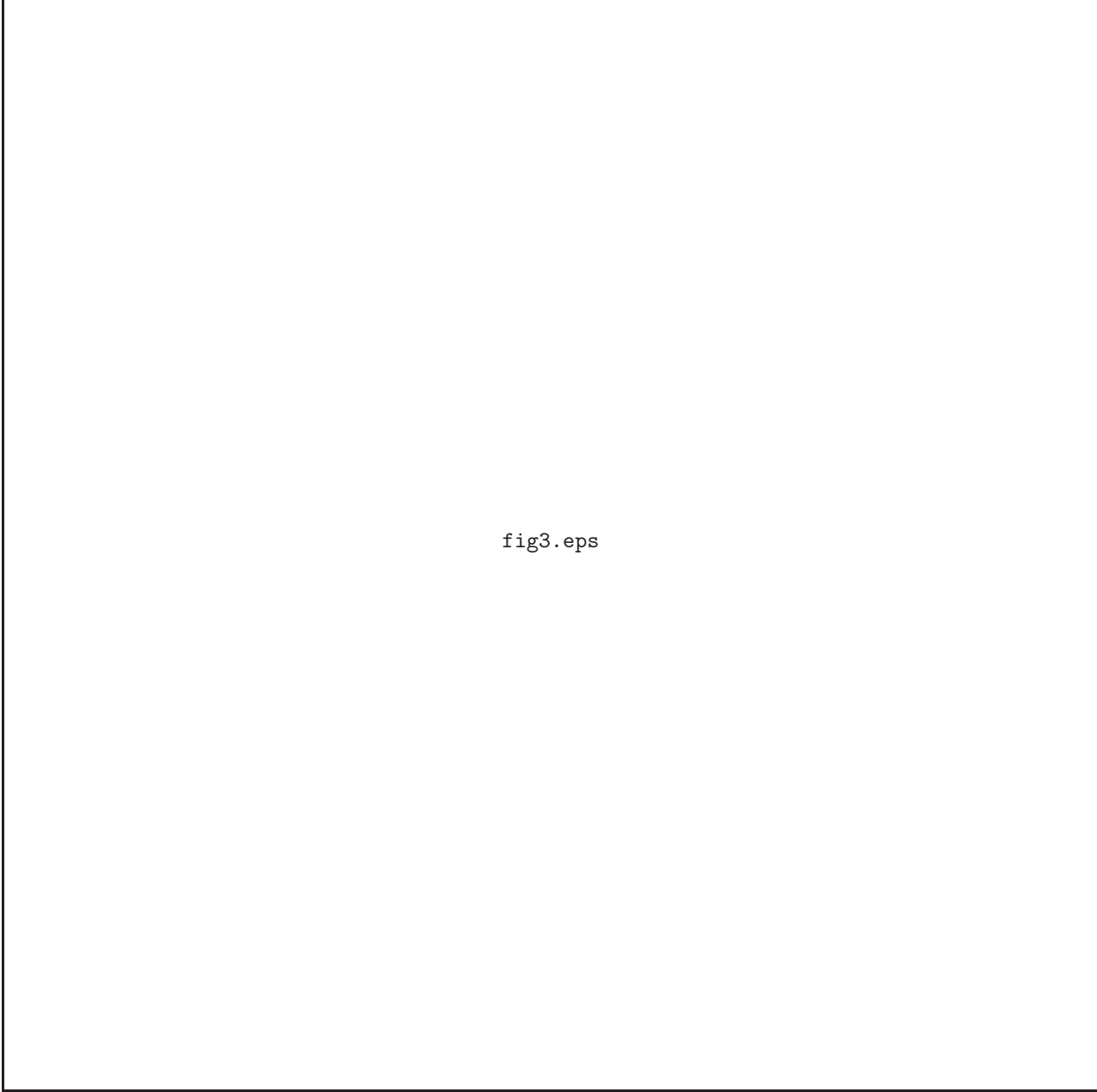
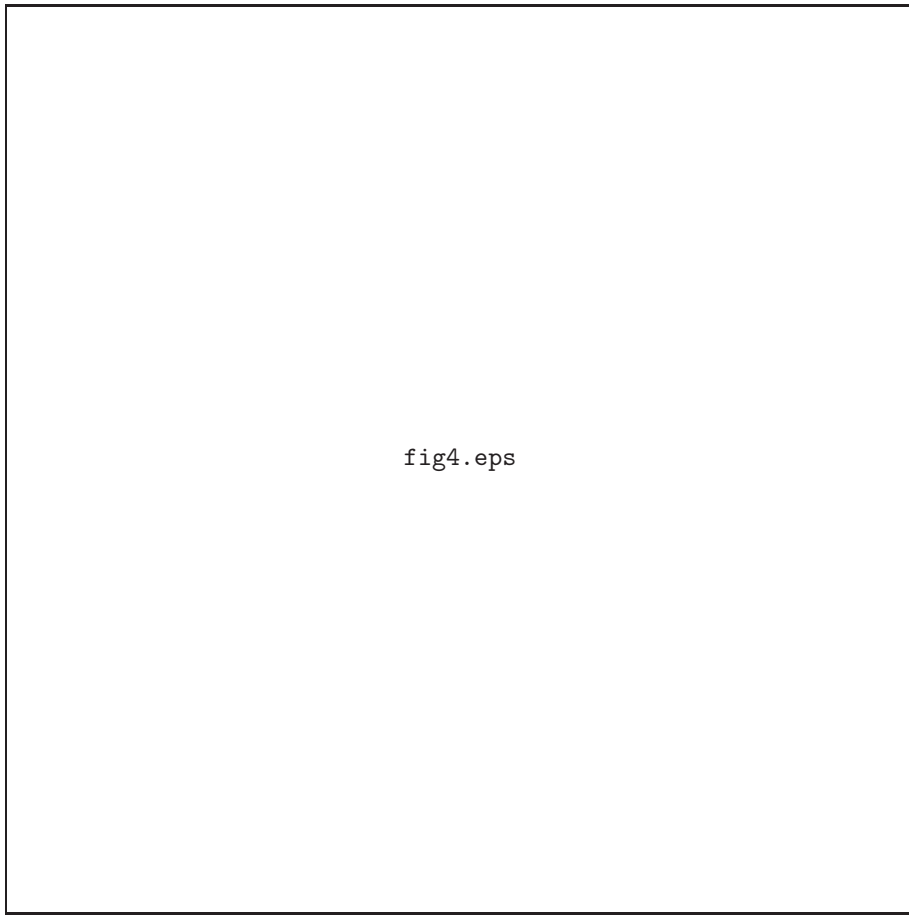
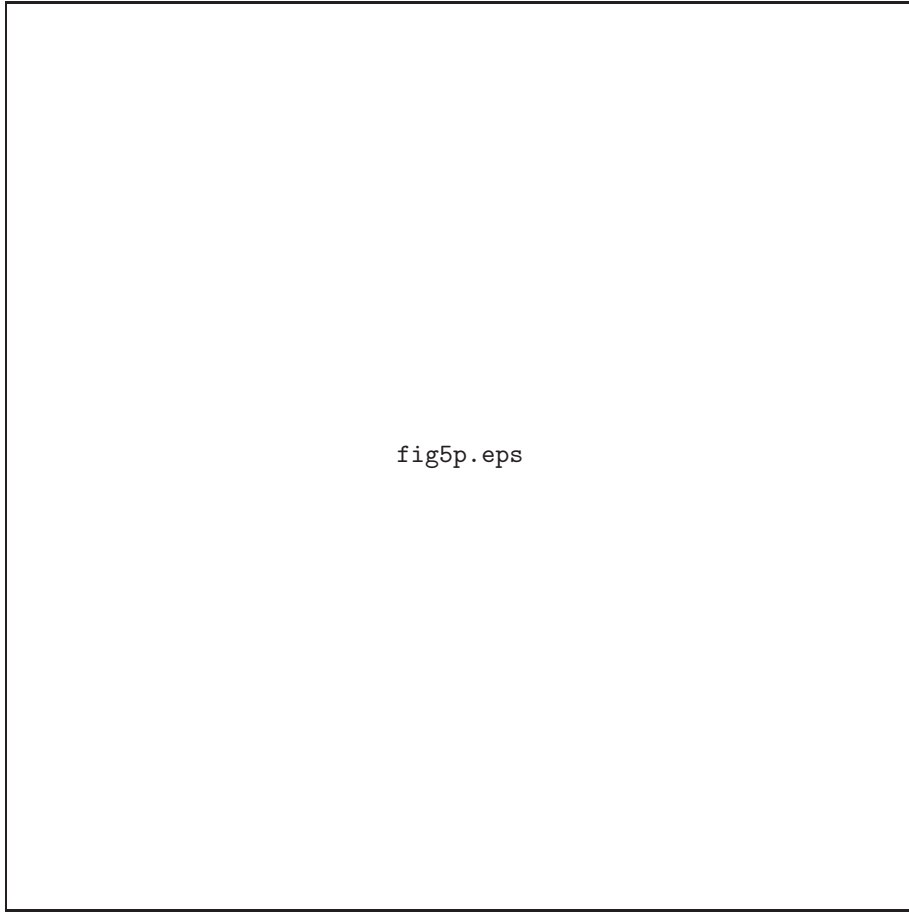


fig3.eps

**Fig. 3.** Temporal evolution of an ideal accretion disk threaded by a poloidal magnetic field. Color levels represent density level (upper panel) and temperature level (bottom panels) while solid lines stand for poloidal magnetic field lines. The time unit labeling each snapshot is for  $t \sim 2\pi \sim 6.28$  corresponds to one Keplerian orbit at  $(r, z) = (1, 0)$ . After a few rotations, outflows are escaping from the disk and the outflow and accretion remain until the last moment of our simulation time



**Fig. 4.** Ratio of  $B_\varphi$  to  $B_p$  along  $r = 0.225$ . at different three time shot, for different magnetic field energy. The twisting magnetic field become more prominent in case of weak magnetic field.



**Fig. 5.** Time variation of the mass outflow rate for three models, the out flow is still intermittent after long time simulation for different initial magnetic field energy

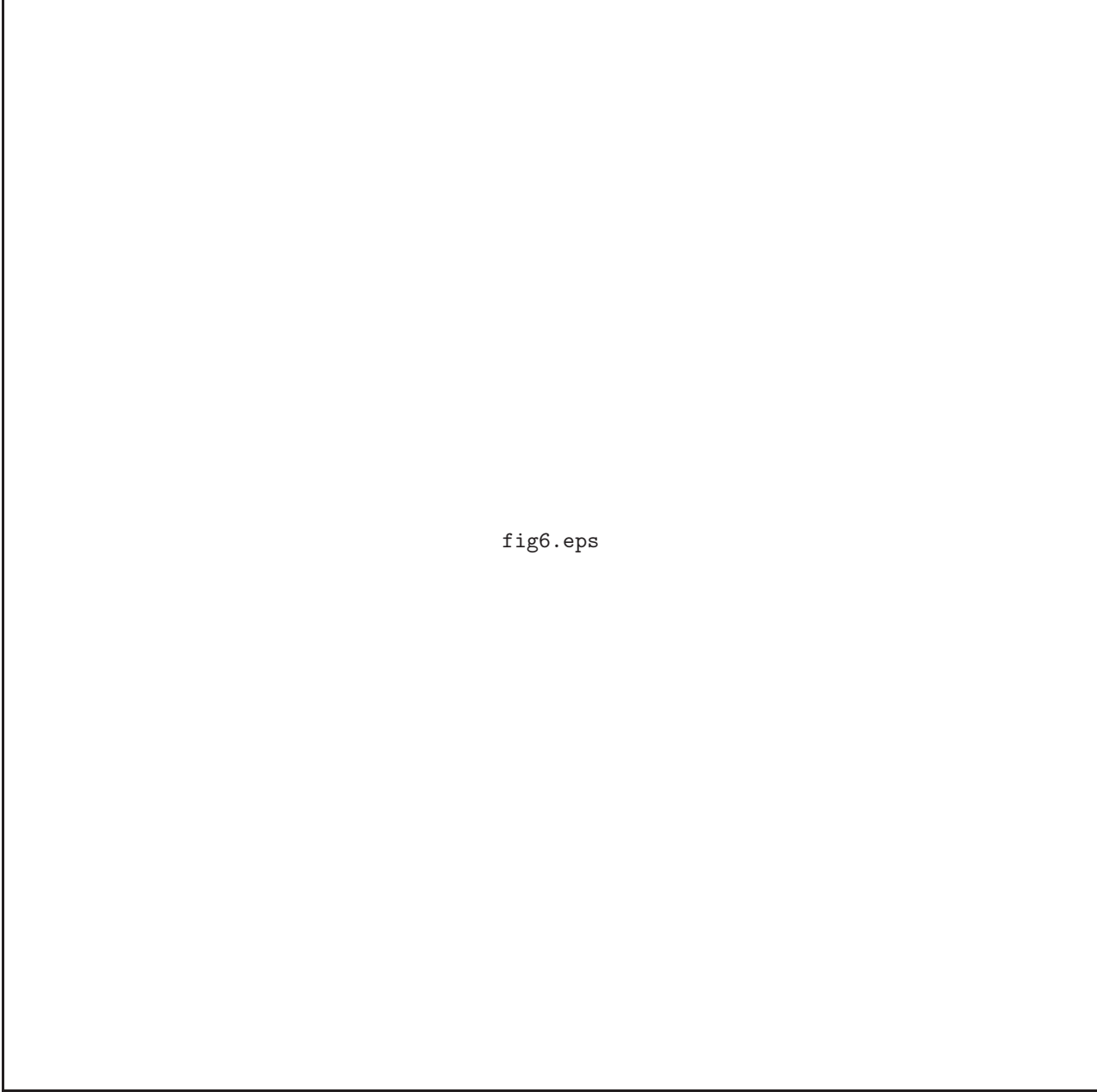


fig6.eps

**Fig. 6.** Time variation of the mass accretion rate for three models, the accretion is still intermittent after long time simulation for different initial magnetic field energy. One Keplerian orbit at  $(r, z) = (1, 0) \sim 2\pi \sim 6.28$  time unit.

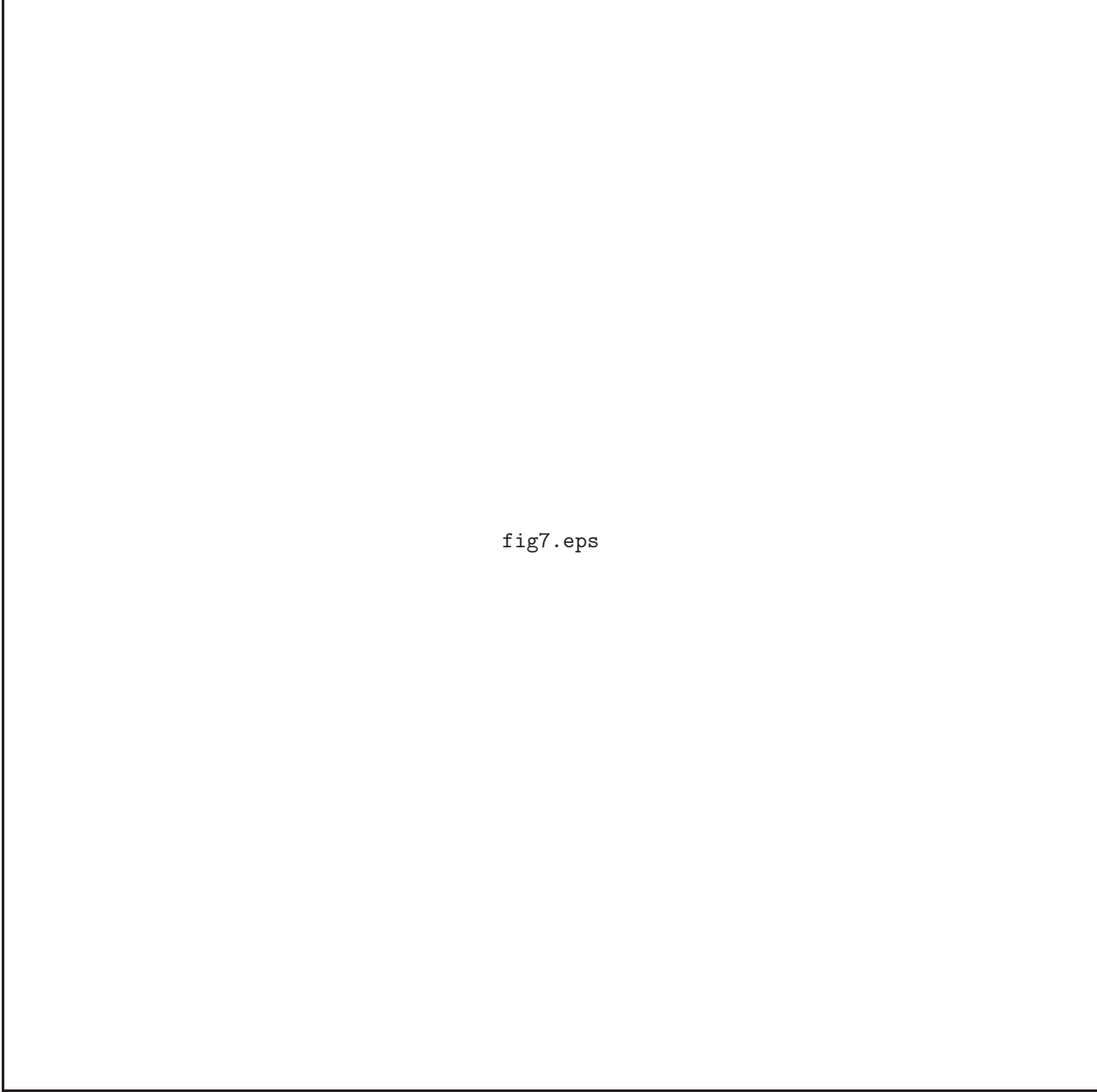


fig7.eps

**Fig. 7.** Accretion rate, averaged between  $r = 0.52$  and  $r = 10$ , against time for different initial magnetic field energy. One Keplerian orbit at  $(r, z) = (1, 0) \sim 2\pi \sim 6.28$  time unit

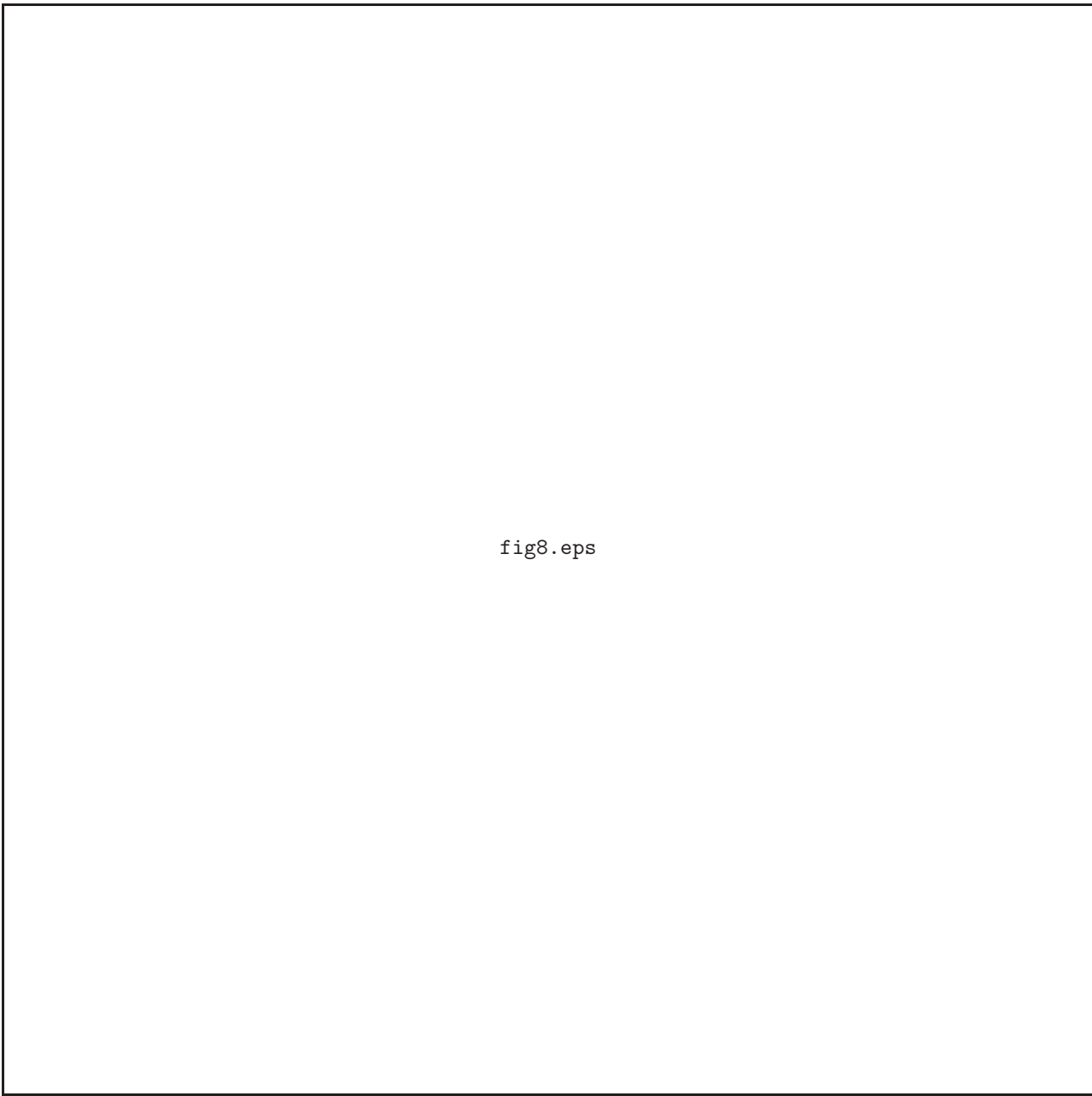


fig8.eps

**Fig. 8.** Accretion rate as a function of radius, for different initial magnetic field, averaged over 10 orbites for models 1, 3, 4 and 6

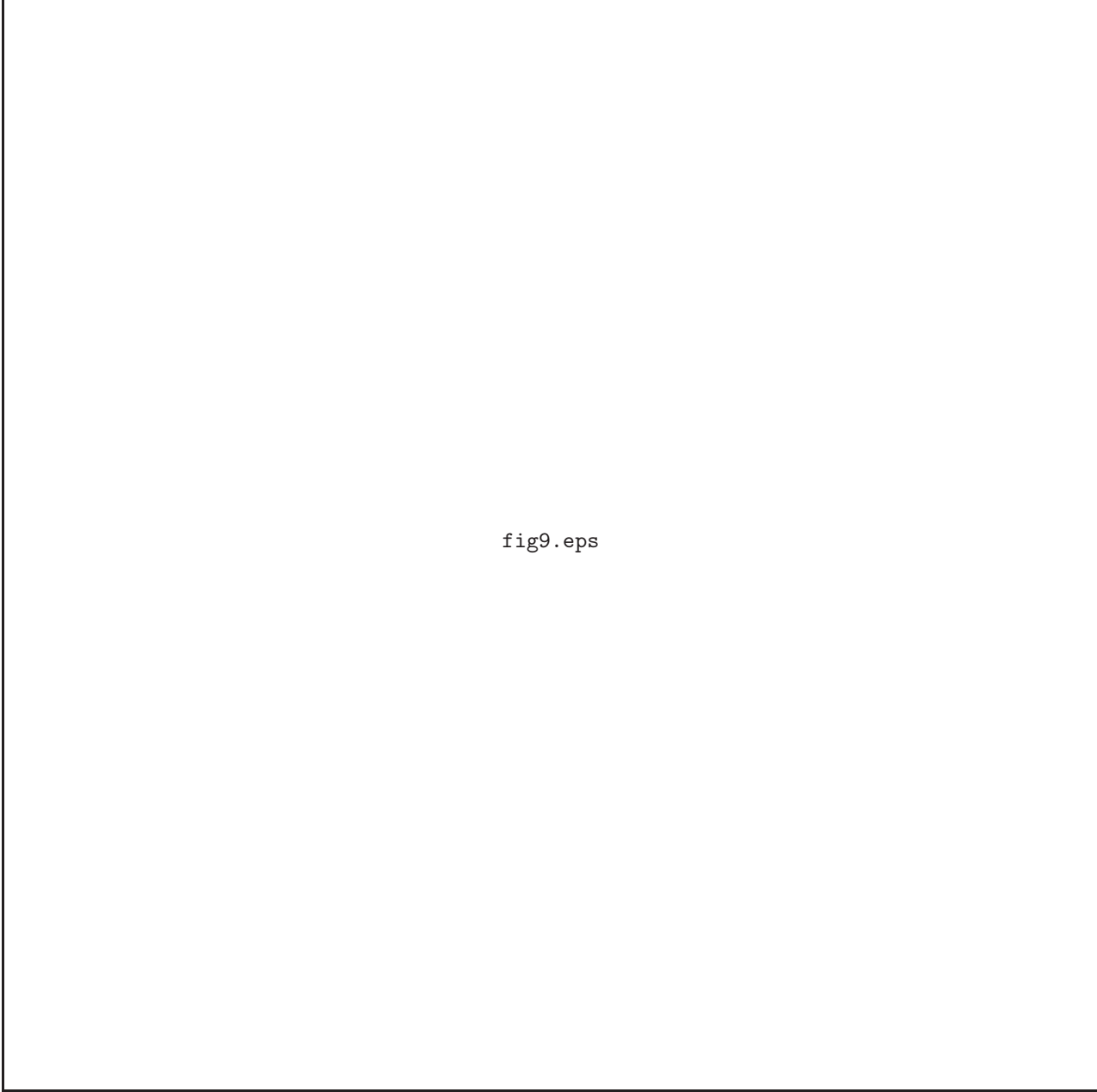


fig9.eps

**Fig. 9.** Time variation of the toroidal energy for three models, the outflow is still intermittent, similar to mass out flow, after long time simulation for different initial magnetic field energy. One Keplerian orbit at  $(r, z) = (1, 0) \sim 2\pi \sim 6.28$  time unit

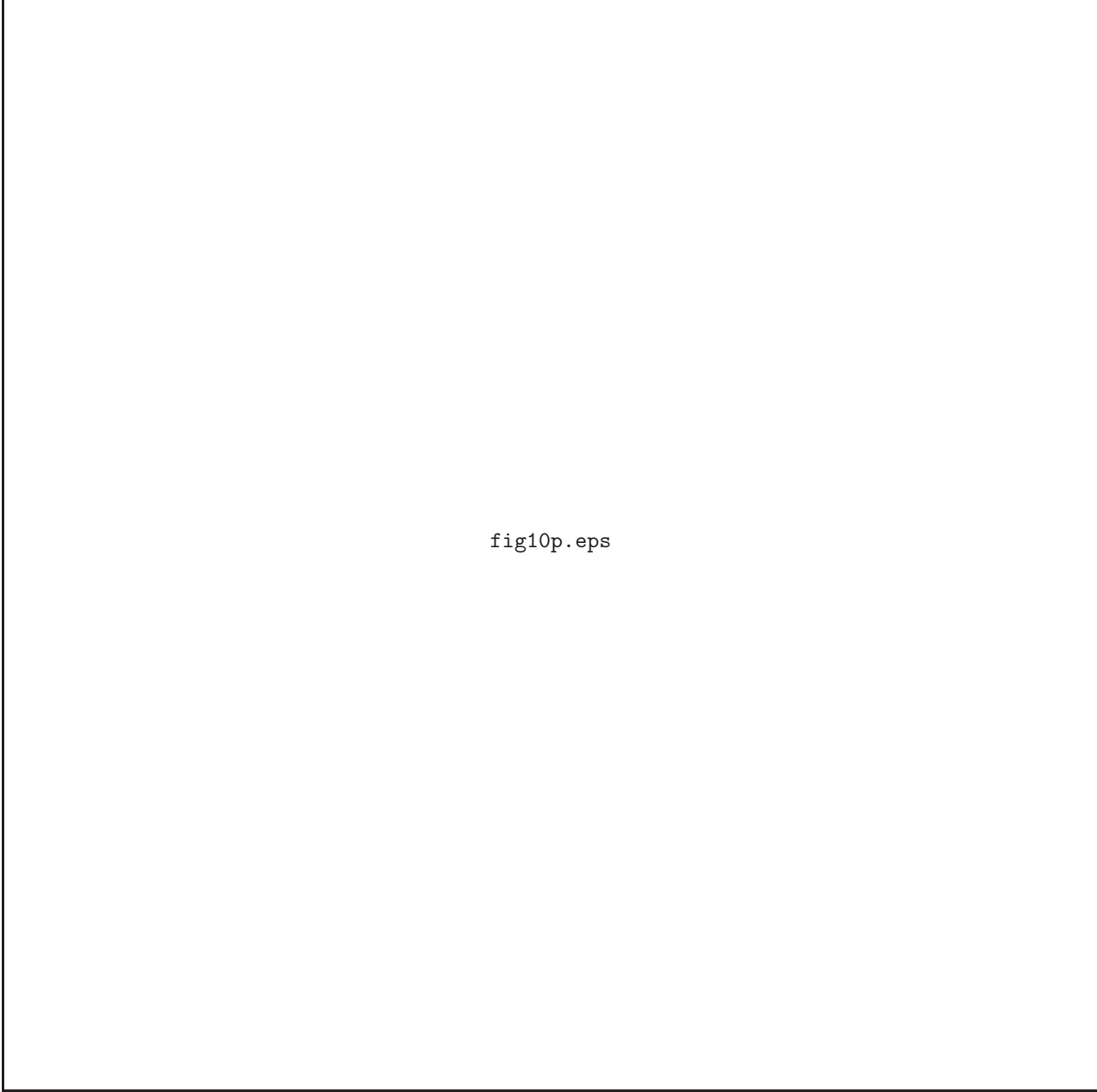


fig10p.eps

**Fig. 10.** The mass flux for four models as a function of time. The numbers correspond to the maximum flux at which we measure the corresponding time (peak time) and plot this time with the initial magnetic field in fig. 11

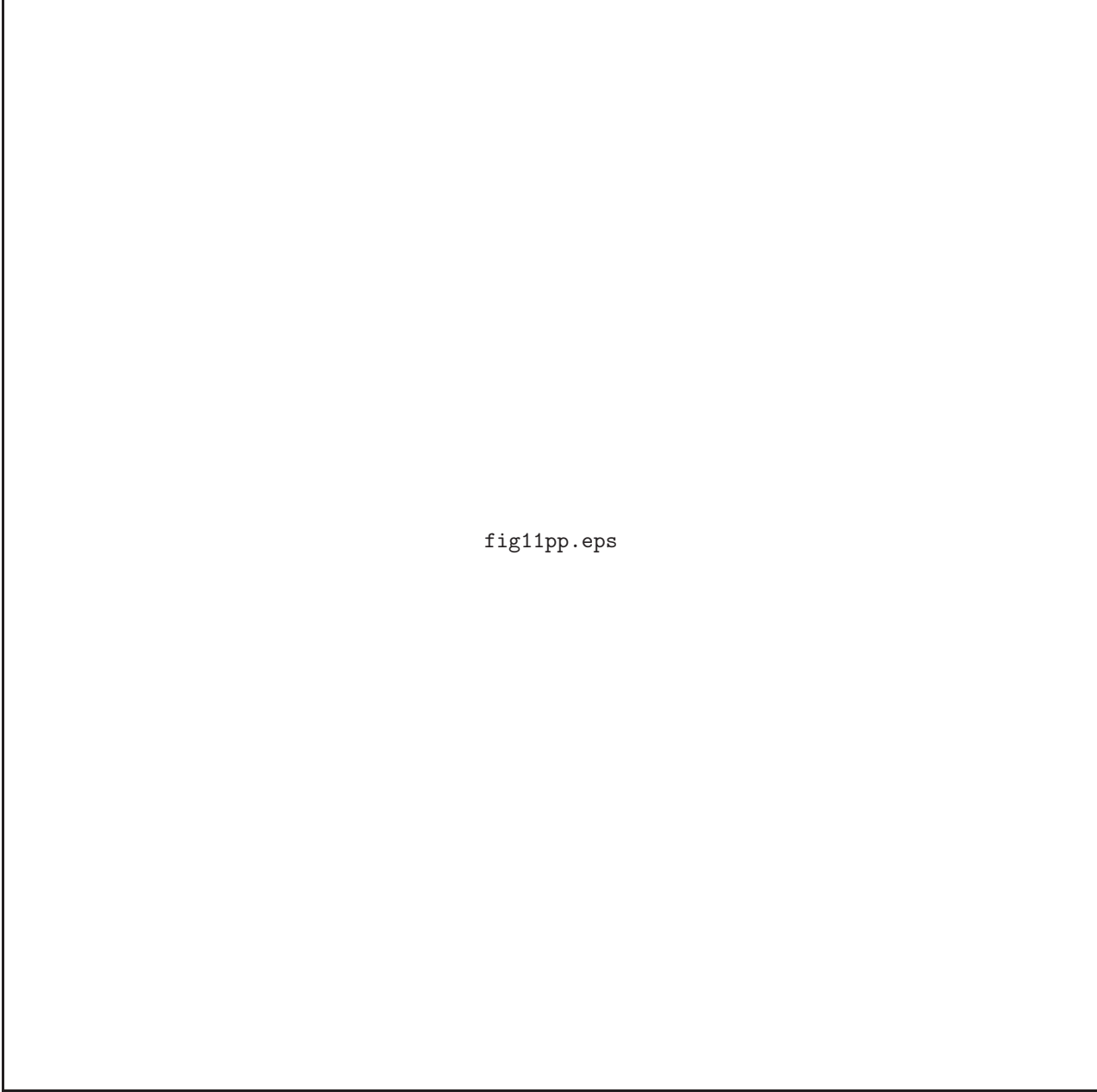


fig11pp.eps

**Fig. 11.** In this figure we show the relation between the average time interval between the mass ejection peaks and the initial magnetic field strength (a) and the average magnetic field (b). Solid line corresponds to the best fit to the numerical result and the dotted line corresponds to the analytical relation ( equation 26).

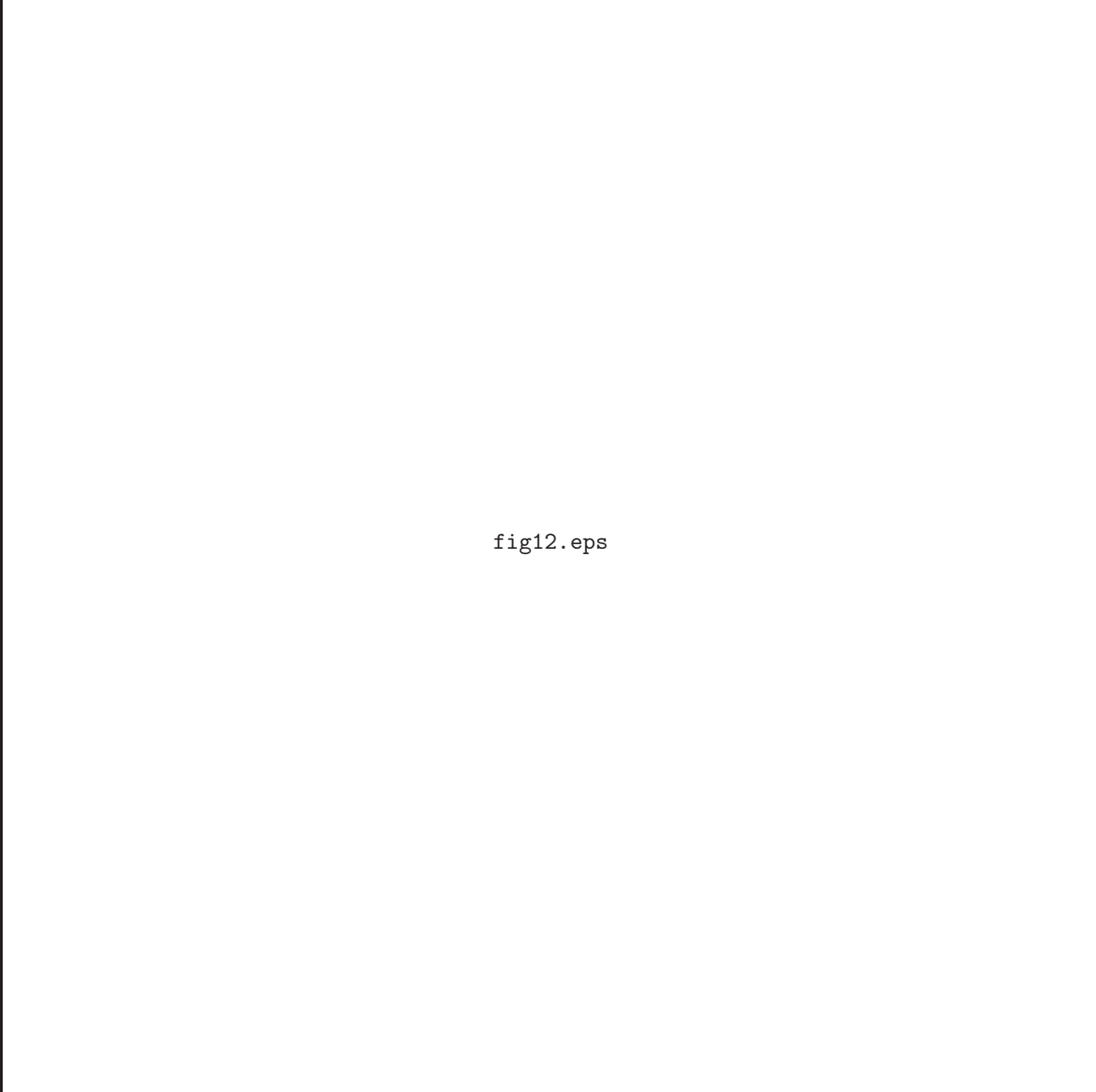


fig12.eps

**Fig. 12.** (a) Time averaged velocities ( $V_{jet \ ave}$ ) as a function of  $E_{mg}$ . (b)  $V_z \ max$  as a function of  $E_{mg}$ . (c) Time averaged velocities( $V_{jet \ ave}$ ) as a function of  $E_{mg}/\dot{M}_w$ . (d)  $V_{jet \ max}$  as a function of  $E_{mg}/\dot{M}_w$ .

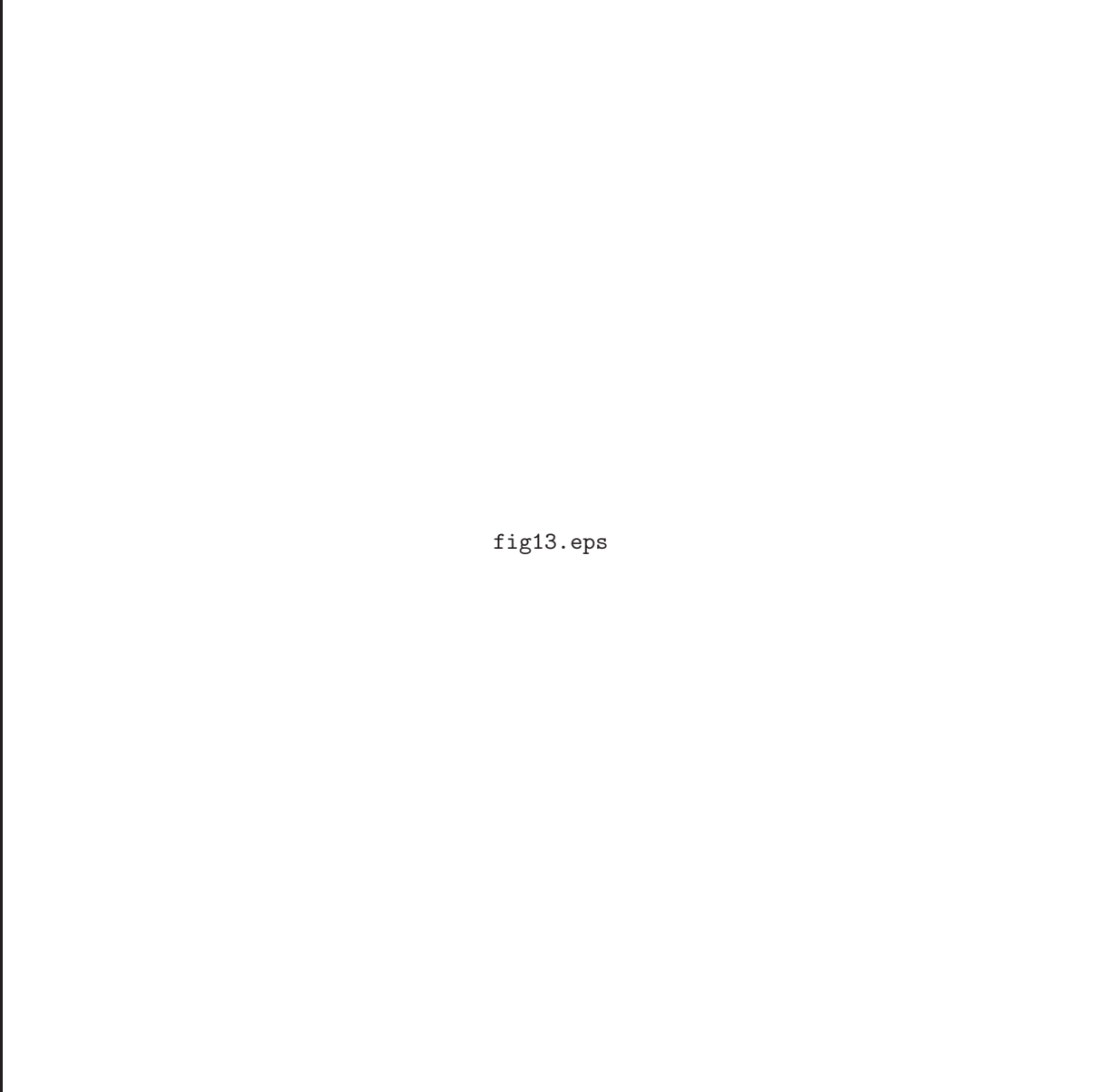
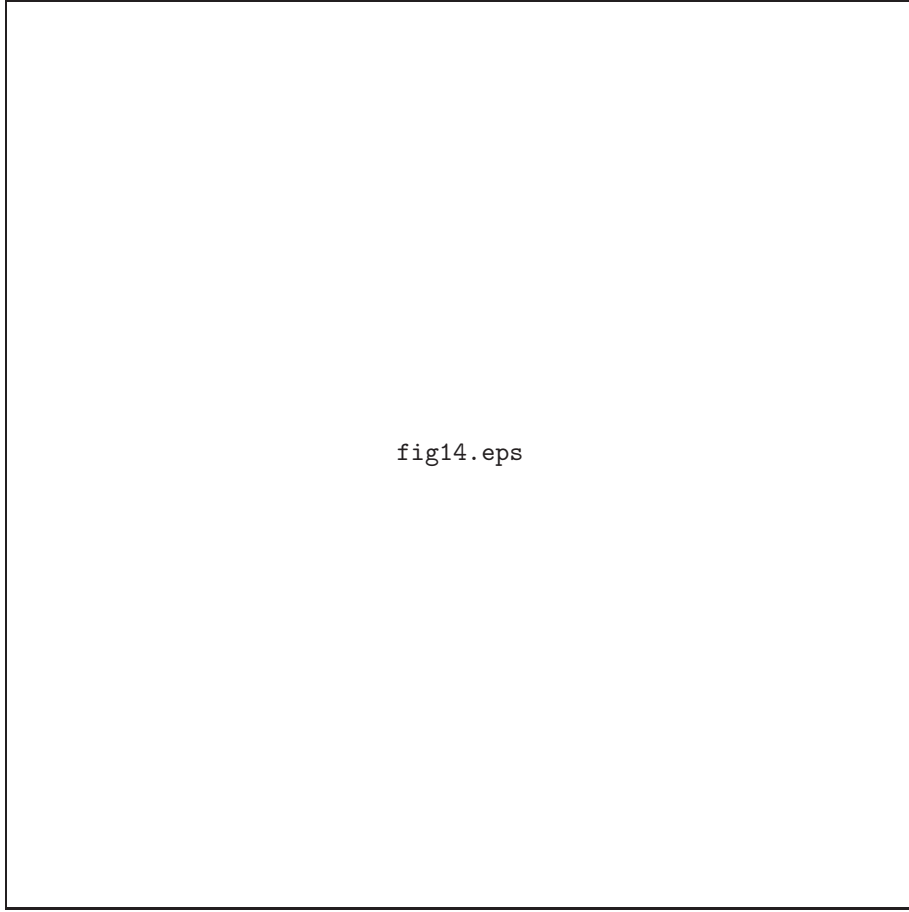
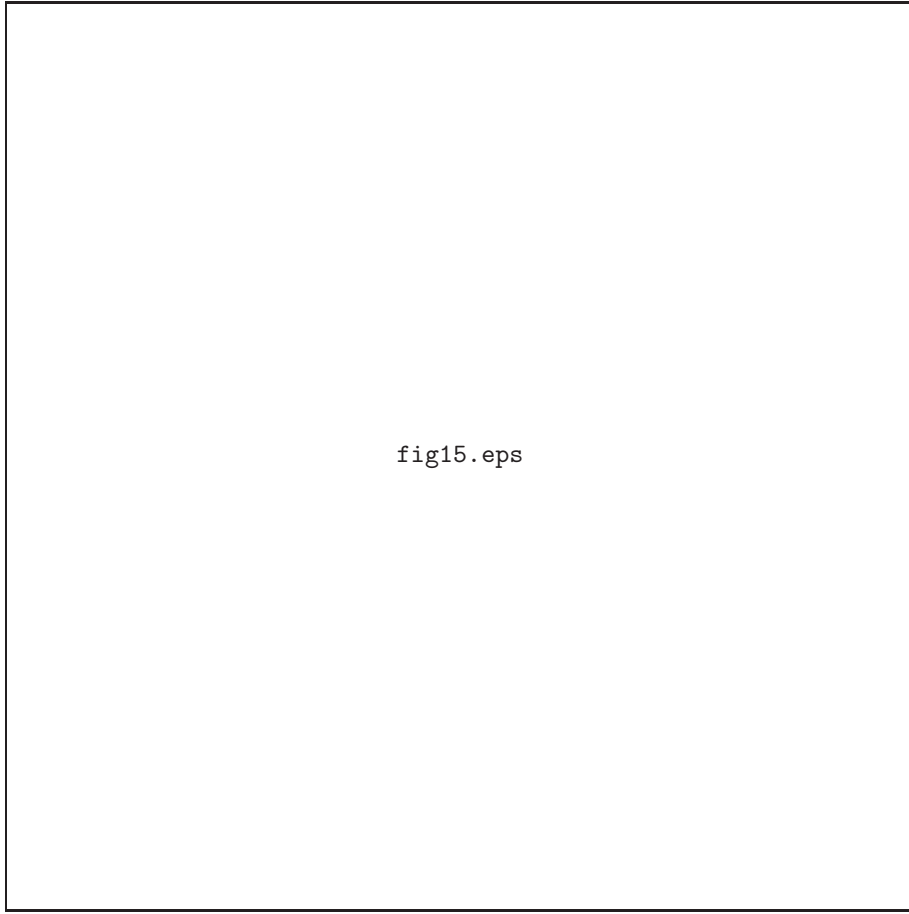


fig13.eps

**Fig. 13.** (a) Time averaged mass accretion ( $\dot{M}_a$ ) rate of the disk as a function of  $E_{\text{mg}}$ . (b) Time averaged mass ejection ( $\dot{M}_w$ ) rate of the jet as a function of  $E_{\text{mg}}$ . (c) Average toroidal ejection ( $E_{mgt}$ ) as a function of  $E_{\text{mg}}$ . (d) The ratio of the time averaged mass outflow rate of the jet to the time averaged mass accretion rate of the disk ( $\dot{M}_w/\dot{M}_a$ ) as a function of  $E_{\text{mg}}$ .



**Fig. 14.** The jet velocity for three models as a function in time. (a) The averaged jet velocity (averaged between  $r=0$  and  $r=1$ ) at height  $z=4$  as a function in time. (b) The maximum jet velocity at  $z=4$  as a function in time (averaged between  $r=0$  and  $r=1$ ). One Keplerian orbit at  $(r,z)=(1,0) \sim 2\pi \sim 6.28$  time unit



**Fig. 15.** Time evolution of powers of the jet; Poynting flux,  $F_{p,j}$  (solid line), thermal flux  $F_{en,j}$  (dashed line), and kinetic flux  $F_{k,j}$  (dotted line) for different initial magnetic field

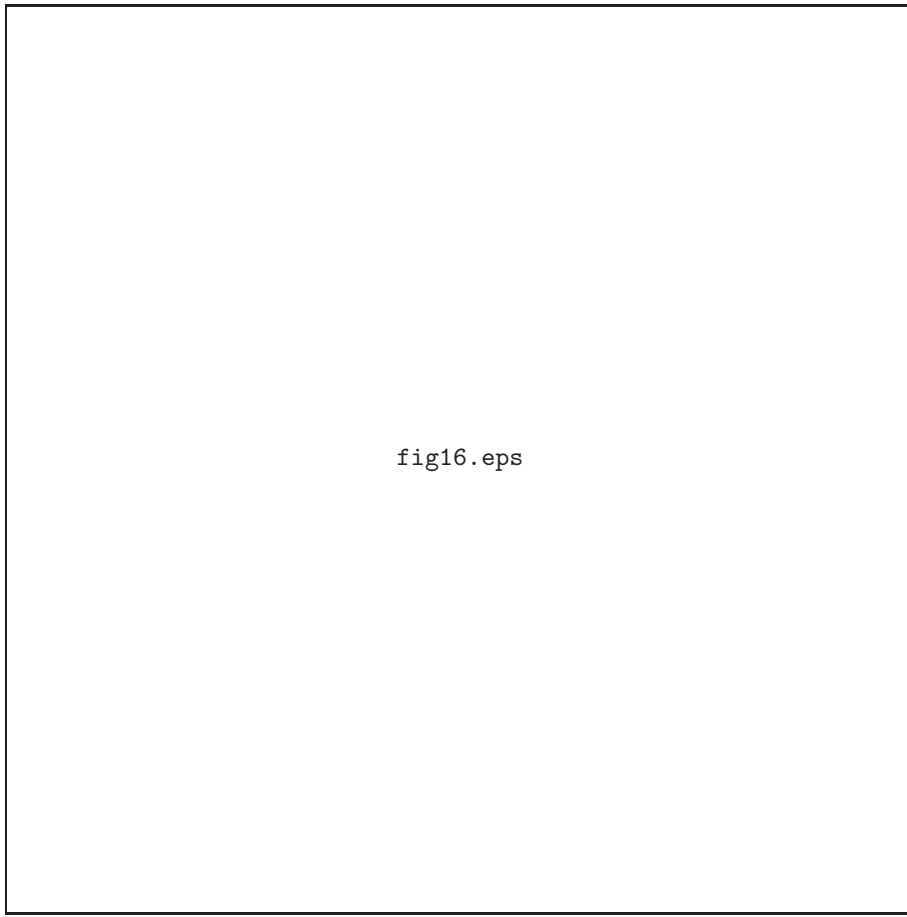


**Fig. 16.** The time average value of enthalpy, kinetic and Poynting flux as a relation with the initial magnetic field strength.

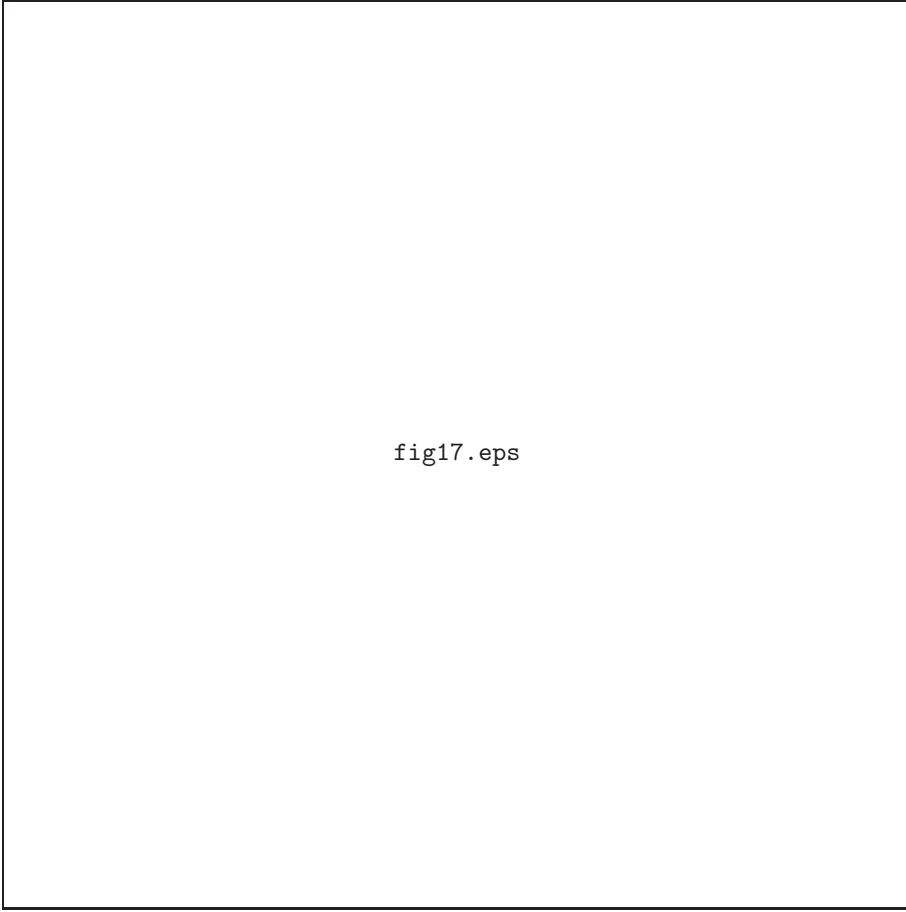


**Fig. 17.** Radial profiles of average physical quantities. The cuts were taken at  $z = 4$ . The radial dependence of density for each initial magnetic field shows that the peak density (which defines the jet) in the first two initial magnetic field is greater than the last weak initial magnetic field case. The radial dependence of the poloidal velocity shows that the collimated flows show higher velocities closer to the disk axis. The radial dependence of the toroidal magnetic field shows that the maximum value is close to the disk axis as expected for collimated jet.

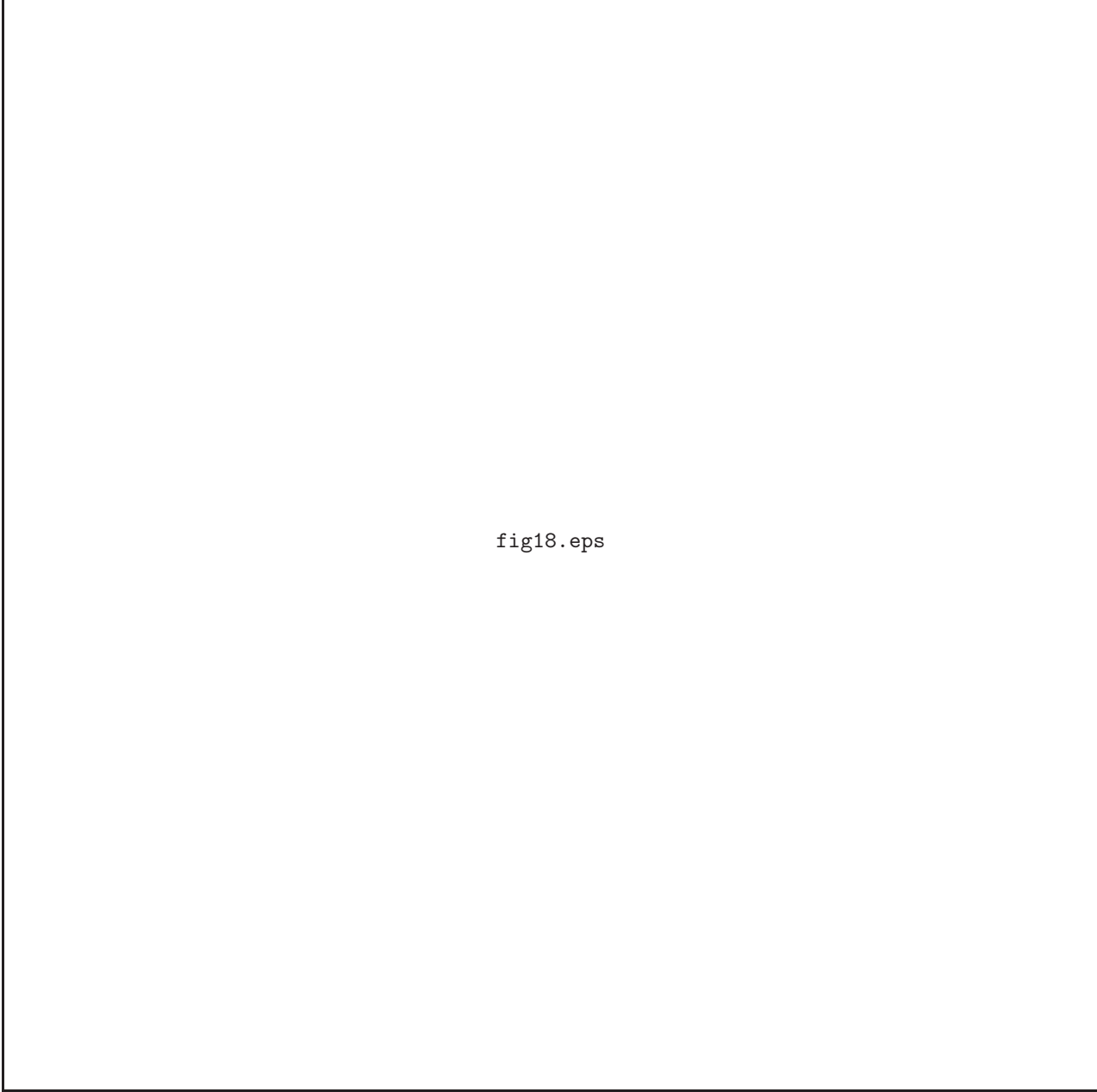
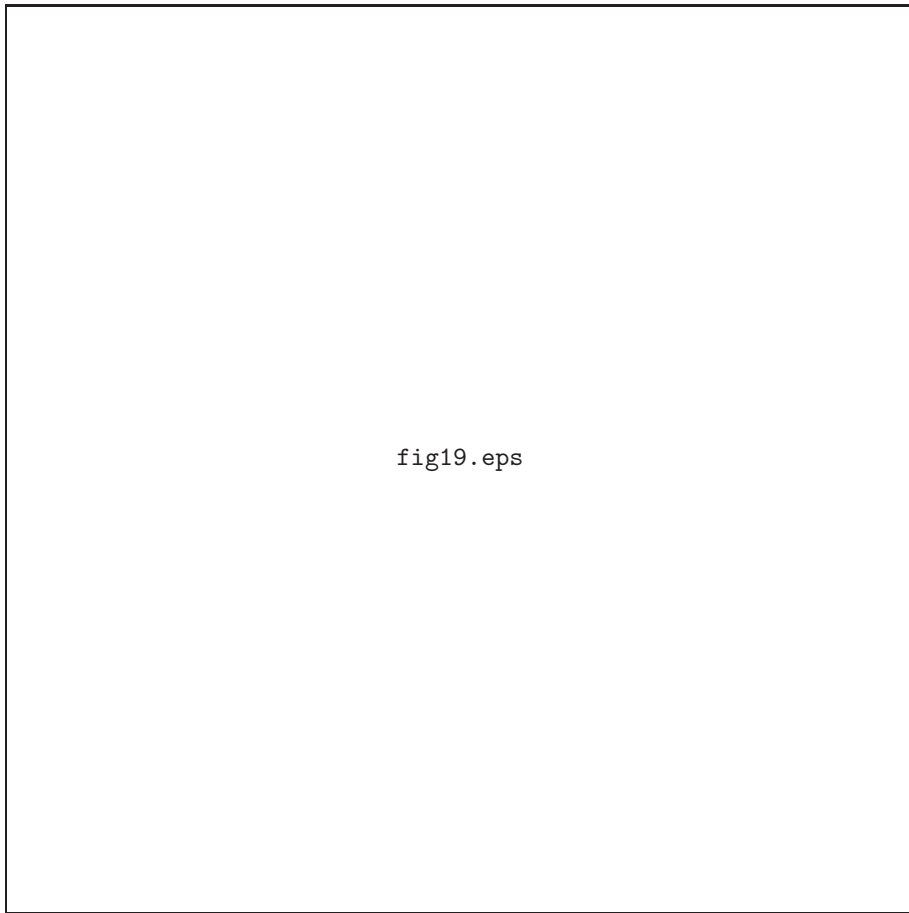


fig18.eps

**Fig. 18.** This figure shows the flux outflow of (a) mass flux ,(b) kinetic flux,(c) toroidal magnetic energy, (d) enthalpy flux, and (e) Poynting flux at  $z=4$  as a function of  $r$ -coordinate. The collimation becomes more clear in case of model 4 in both mass flux and kinetic flux



**Fig. 19.** The lines represent the progress of the maximum of different fluxes in z-direction. The collimation begins at low-z in case of strong initial magnetic field.

This figure "fig1.jpg" is available in "jpg" format from:

<http://arxiv.org/ps/0704.2918v1>

This figure "fig2.jpg" is available in "jpg" format from:

<http://arxiv.org/ps/0704.2918v1>

This figure "fig3.jpg" is available in "jpg" format from:

<http://arxiv.org/ps/0704.2918v1>

This figure "fig4.jpg" is available in "jpg" format from:

<http://arxiv.org/ps/0704.2918v1>

This figure "fig5p.jpg" is available in "jpg" format from:

<http://arxiv.org/ps/0704.2918v1>

This figure "fig6.jpg" is available in "jpg" format from:

<http://arxiv.org/ps/0704.2918v1>

This figure "fig7.jpg" is available in "jpg" format from:

<http://arxiv.org/ps/0704.2918v1>

This figure "fig8.jpg" is available in "jpg" format from:

<http://arxiv.org/ps/0704.2918v1>

This figure "fig9.jpg" is available in "jpg" format from:

<http://arxiv.org/ps/0704.2918v1>

This figure "fig10p.jpg" is available in "jpg" format from:

<http://arxiv.org/ps/0704.2918v1>

This figure "fig11pp.jpg" is available in "jpg" format from:

<http://arxiv.org/ps/0704.2918v1>

This figure "fig12.jpg" is available in "jpg" format from:

<http://arxiv.org/ps/0704.2918v1>

This figure "fig13.jpg" is available in "jpg" format from:

<http://arxiv.org/ps/0704.2918v1>

This figure "fig14.jpg" is available in "jpg" format from:

<http://arxiv.org/ps/0704.2918v1>

This figure "fig15.jpg" is available in "jpg" format from:

<http://arxiv.org/ps/0704.2918v1>

This figure "fig16.jpg" is available in "jpg" format from:

<http://arxiv.org/ps/0704.2918v1>

This figure "fig17.jpg" is available in "jpg" format from:

<http://arxiv.org/ps/0704.2918v1>

This figure "fig18.jpg" is available in "jpg" format from:

<http://arxiv.org/ps/0704.2918v1>

This figure "fig19.jpg" is available in "jpg" format from:

<http://arxiv.org/ps/0704.2918v1>